Atmospheric Environment 342 (2025) 120918

Contents lists available at ScienceDirect

Atmospheric Environment

journal homepage: www.elsevier.com/locate/atmosenv

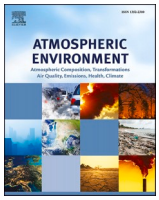

Environmental drivers of tropospheric bromine and mercury variability in coastal East Antarctica

Neil C. Page [a,b,**], Jenny A. Fisher [a,*], Stephen R. Wilson [a], Robyn Schofield [c], Robert G. Ryan [c], Sean Gribben [d], Andrew R. Klekociuk [e], Grant C. Edwards [f], Anthony Morrison [f]

[a] Centre for Atmospheric Chemistry, School of Earth, Atmospheric and Life Sciences, University of Wollongong, Wollongong, NSW, Australia
[b] Sustainability & Climate Change, Deloitte Risk Advisory Pty Ltd, Sydney, Australia
[c] School of Geography, Earth and Atmospheric Sciences, University of Melbourne, Melbourne, Vic, Australia
[d] CSIRO, Oceans and Atmospheres, Aspendale, Vic, Australia
[e] Australian Antarctic Division, Kingston, Tasmania, Australia
[f] School of Natural Sciences, Faculty of Science and Engineering, Macquarie University, Sydney, NSW, Australia

HIGHLIGHTS

- Three modes dominate chemical-meteorological variability in coastal east Antarctica.
- The modes represent vertical mixing, blowing snow, and ocean sources.
- The three modes explain significant variability in tropospheric bromine and mercury.

ARTICLE INFO

Keywords:
Tropospheric chemistry
Bromine
Mercury
Antarctica
Southern ocean
Sea ice

ABSTRACT

Bromine radicals released from sea ice, snow, and marine sources play a critical role in the atmospheric chemistry of polar regions. The Chemical and Mesoscale Mechanisms of Polar Cell Aerosol Nucleation (CAMMPCAN) ship campaign conducted in coastal East Antarctica over two 6-month periods in 2017–18 and 2018–19 provides a unique dataset to identify the environmental drivers of bromine variability in Antarctic spring and summer. In this study, we used CAMMPCAN chemical and meteorological observations combined with reanalysis data from the Modern Era Retrospective Analysis for Research and Applications version 2 (MERRA-2) and satellite-based sea ice data from the National Snow and Ice Data Center to select variables that showed statistically significant correlation with bromine monoxide (BrO) partial columns measured during CAMMPCAN. We then used those variables in principal component analysis and subsequent principal component regression to identify dominant modes of Antarctic environmental variability and their impacts on lower tropospheric BrO. Comparing our three dominant Antarctic principal components to those from a similar analysis conducted previously for the Arctic (Swanson et al., 2020), we found only one mode with clear overlap, representing a vertical mixing mode in which low-pressure systems mix BrO and its precursors into the lower troposphere. We also identified an Antarctic mode describing conditions favourable for blowing snow, similar to the combined effect of two modes from the Arctic analysis but more clearly disambiguated here due to the inclusion of sea ice data in our analysis. The third Antarctic mode, attributed to an ocean source (biological activity and/or sea salt aerosol), was particularly important in summer. The principal component regression model developed from these modes showed moderate skill in predicting BrO partial columns in the lowest 2 km of the troposphere ($R = 0.51$), a significant improvement over the Arctic-based regression model ($R = 0.08$). Neither model could reproduce the observed variability in BrO in the lowest 200 m. Finally, we applied the same analysis to coincident CAMMPCAN observations of gaseous elemental mercury and found regression of our three dominant modes could explain nearly 50% of observed mercury variability ($R = 0.69$). Our results reinforce the importance of sea ice and ocean processes in bromine cycling in coastal East Antarctica and highlight the need to consider Antarctic-specific processes in mechanistic models of atmospheric bromine chemistry.

* Corresponding author. Northfields Avenue, University of Wollongong, Wollongong, NSW, 2522, Australia.
** Corresponding author. Northfields Avenue, University of Wollongong, Wollongong, NSW, 2522, Australia.
E-mail addresses: npage87@yahoo.com.au (N.C. Page), jennyf@uow.edu.au (J.A. Fisher).

https://doi.org/10.1016/j.atmosenv.2024.120918
Received 14 June 2024; Received in revised form 28 October 2024; Accepted 31 October 2024
Available online 8 November 2024

1. Introduction

Seasonal sea ice plays an important role in the production and distribution of tropospheric bromine in polar regions. Every spring, high concentrations of reactive bromine are rapidly released to the Antarctic troposphere by the production of molecular bromine (Br_2) via heterogenous reactions on sea ice surfaces (Prados-Roman et al., 2018). The gaseous Br_2 is then photolyzed to form bromine radicals (Br) which react with ozone (O_3) to form bromine monoxide (BrO) (Herrmann et al., 2019). This series of chemical reactions, known as a bromine explosion, rapidly depletes tropospheric O_3 and oxidises gaseous elemental mercury (Hg^0), affecting the chemistry and oxidising capacity of the polar troposphere and depositing toxic water-soluble mercury into the polar environment (Simpson et al., 2015). The combined effects of increasing anthropogenic mercury (Fisher et al., 2023; Pang et al., 2022), warming temperatures, and changes to sea ice cover from climate change may be negatively impacting Antarctic ecosystems. Given the remoteness and limited accessibility of the Antarctic sea ice region, the environmental mechanisms that control bromine cycling and the implications for mercury cycling remain poorly characterised. Here, we identify key environmental drivers using a novel dataset of ship-based measurements collected in the Antarctic sea ice region over two field seasons.

The process of sea ice formation in polar regions helps to concentrate sea salts within brine pockets, resulting in freshly formed first-year sea ice (and the brine-rich snow layer on this first-year sea ice) having a high surface salinity and therefore being particularly important for bromine production (Vancoppenolle et al., 2006). The brine pockets are also important for mercury methylation and provide a large source of methylated mercury to the ocean during sea ice melt (Gionfriddo et al., 2016). The variability of the mole fraction of BrO in polar regions is affected by meteorological and environmental parameters including sea surface salinity, temperature, pH, sea ice cover, O_3 mixing ratio and relative humidity, as identified by laboratory experiments (Halfacre et al., 2019), field measurements (Pratt et al., 2013), satellite observations (Seo et al., 2020) and modeling (Huang et al., 2020; Huang and Jaeglé, 2017; Rhodes et al., 2017). Uncertainties remain in the relative importance of these parameters and the processes by which they influence BrO variability, particularly across the diverse geographies of the Antarctic (Frieβ et al., 2023; Wagh et al., 2023).

Ground-based observations can provide insights into the relative importance of different drivers of BrO variability, and whether these vary across different environments. However, ground-based observations of tropospheric BrO in Antarctica are mostly limited to a handful of short-term campaigns and a small number of Antarctic stations (Wagh et al., 2023). The longest continuous records of tropospheric BrO in Antarctica come from Neumayer (2003–2021) and Arrival Heights (2012–2021) (Frieβ et al., 2023). Past studies indicate strong seasonal variability in Antarctic BrO, with the highest concentrations typically observed during spring and the maximum occurring immediately following polar sunrise (Prados-Roman et al., 2018). Enhanced BrO levels during spring have been linked to extended air mass contact with first-year sea ice (Wagh et al., 2023). Observations at Neumayer also indicate a strong aerosol-BrO correlation, with BrO levels during summer and autumn dependent on meteorological conditions and air mass residence time over the sea ice, snowpack and open ocean (Frieβ et al., 2023). The representativeness of these relationships across coastal Antarctica remains uncertain due in part to the limited spatial extent of the existing ground-based datasets.

A major challenge of identifying process-based drivers of BrO variability comes from the complex interactions between multiple meteorological and chemical parameters that are themselves correlated with one another (Frieβ et al., 2023). Statistical dimensionality reduction methods provide a useful framework for addressing this challenge. For example, Swanson et al. (2020) related the mole fraction of Arctic BrO to meteorological variables by using a principal component analysis (PCA) to infer three dominant modes of Arctic variability based on aerosol extinction observations, surface meteorological and in situ O_3 observations, and reanalysis meteorological data. From there, they developed a principal component regression (PCR) model for predicting BrO in the Arctic lower troposphere and found that the three dominant meteorological and chemical modes could explain 60% of the variance in the Arctic BrO data. This model has never been applied to the Antarctic, and it remains unclear whether the identified factors represent fundamental physical processes that apply to polar regions broadly or whether they are specific to the Arctic. It also remains unclear whether there are additional modes of variability that are unique to the Antarctic region. While the processes described above occur in both the Arctic and Antarctic, there are additional factors that are unique to the Antarctic, such as very high levels of iodine monoxide (Frieβ et al., 2010; Saiz-Lopez et al., 2007), necessitating Antarctic-specific analysis of BrO variability. Atmospheric mercury cycling, too, differs between the polar regions, with the Antarctic less affected than the Arctic by transported mercury emissions from the midlatitudes but more affected by katabatic airflow and chemical reactivity over the ice sheet (Angot et al., 2016a).

In this study, we use data from the Chemical and Mesoscale Mechanisms of Polar Cell Aerosol Nucleation (CAMMPCAN) field campaign to identify the primary environmental variables driving BrO and Hg^0 variability in the coastal East Antarctic. Sections 2 and 3 describe the data sources and methods used to identify the most relevant environmental drivers. Section 4 presents results and discussion, starting with characterising the dataset (Section 4.1) and testing the applicability of the Swanson et al. (2020) Arctic model to prediction of Antarctic BrO partial columns (Section 4.2). From there, we identify the statistical modes of environmental variability in the Antarctic (Section 4.3) and use these to develop a new predictive BrO model specific to the Antarctic (Section 4.4). We then apply the same methodology to prediction of Antarctic Hg^0 (Section 4.5). Finally, Section 5 provides a summary and conclusion.

2. Data sources

In this section, we describe the datasets used for analysis, including data from the CAMMPCAN field campaign (Section 2.1), meteorological reanalysis data (Section 2.2), back trajectories (Section 2.3), and sea ice data (Section 2.4).

2.1. CAMMPCAN chemical and meteorological observations

The CAMMPCAN campaign involved eight ship-based resupply voyages aboard the RSV Aurora Australis to the Southern Ocean between October 2017 and March 2019 (Schofield and Ryan, 2021a, 2021b). Data selected for this analysis are from the six voyages that visited the Australian Antarctic Division (AAD) research stations of Davis, Casey and Mawson on the coast of east Antarctica (the remaining two voyages went to Macquarie Island in the sub-Antarctic and did not enter the sea ice region). All CAMMPCAN data are available at https://data.aad.gov.au/. A list of shipboard measurements and measurement heights is provided in Table S1, with the locations of observational equipment aboard RSV Aurora Australis shown in Fig. S1.

The voyage routes are shown in Fig. 1. Only data collected when the ship was docked on station (at Davis, Casey, or Mawson) or otherwise located within the sea ice (defined by the presence of sea ice at the location of the ship, using the satellite dataset described in Section 2.4) were included in the analysis. The periods of sea ice filtered observations from each voyage are detailed in Table S2.

2.1.1. MAX-DOAS retrievals of BrO, aerosol extinction coefficient, and NO_2

BrO and nitrogen dioxide (NO_2) observations at 20-min time resolution were retrieved using Multi-AXis-Differential Optical Absorption Spectroscopy (MAX-DOAS) (Hönninger and Platt, 2002). Our MAX-DOAS instrument used a scan pattern of 12 elevation angles (−3,

−2, −1, 0, 1, 2, 3, 5, 10, 20, 40, 90°) to collect spectral information. Due to ocean swell affecting the angular stability of the MAX-DOAS instrument, at each elevation multiple spectra were collected at a frequency of 1 Hz with the actual observation angle recorded, and stable observations binned into the above categories. These spectra were fitted with relevant trace gas cross sections, including BrO and NO_2, using the software QDOAS (Danckaert et al., 2017) with the 90° spectrum closest in time to each low elevation angle observation used as the reference. The output of this process are differential slant column densities. Vertical BrO profiles from this scan pattern were retrieved using the optimal estimation algorithm HEIPRO, an updated version of the algorithm described by Frieβ et al. (2006, 2011), with the SCIATRAN radiative transfer model version 2.1.5 (Rozanov et al., 2014). For our BrO retrievals, we used an *a priori* vertical profile that exponentially decreases with altitude and uses a surface value of 1 pptv, as used by Hay (2011), and analysis settings described by Simpson et al. (2017). The aerosol extinction coefficient (AEC) in the lowest 200 m and lower tropospheric aerosol optical thickness were retrieved from MAX-DOAS measurements of O_4 collisional dimer by methods analogous to those used by Frieβ et al. (2011), Peterson et al. (2015), and Simpson et al. (2017). The vertical profile of BrO in the lower troposphere is best represented by two quantities: the vertical column density of BrO in the lowest 200 m (BrO_{surf}) and the vertical column density of BrO in the lowest 2000 m of the troposphere (BrO_{LTcol}) (Peterson et al., 2015). Units for these partial vertical columns are molecules cm^{-2}. For NO_2, a full profile analysis was not performed, but a high value of the differential slant column density (dSCD) at 2° was used as evidence of local air pollution (see Section S2.4 in the supplement).

2.1.2. *In situ measurements of Hg^0 and O_3*

Gaseous elemental mercury (Hg^0) was measured using a Tekran™ gas-phase ambient mercury analyser (model 2537A) with an inlet height of ~18.5 m above sea level (ASL). The analyser operated at 5-min time resolution with a 1.0 L min^{-1} airflow rate. The sampled air was prefiltered through a polytetrafluorethylene (PTFE) filter and soda lime trap to scrub reactive mercury, acids and organic aerosols. The scrubbed air was then passed over one of two gold cartridges (traps). While one trap captured Hg^0, the other was heated to 500 °C to thermally desorb the Hg^0 into an inert carrier gas (Argon) that carried it for analysis via cold vapor atomic fluorescence spectrometry (CVAFS) at 253.7 nm (Steffen et al., 2012).

O_3 was measured at a 1-min time resolution. For the 2017–18 voyages, O_3 was measured using a dual absorption cell ultraviolet ozone monitor run by the U.S. Department of Energy Atmospheric Radiation Measurement (ARM) facility as part of its MARCUS (Measurements of Aerosols, Radiation, and Clouds over the Southern Ocean) campaign (U.S Department of Energy's Atmospheric Radiation Measurement program, 2019). For the 2018–19 voyages, O_3 was measured using a commercial ThermoFisher O_3 monitor situated inside the Atmospheric Integrated Research facility for Boundaries and Oxidative eXperiments (AIRBOX) mobile laboratory (AIRBOX, 2019).

2.1.3. *Meteorological observations and underway data*

Wind speed and wind direction were obtained from two wind anemometers located on separate masts (on the port and starboard sides of the RSV Aurora Australis) at a height of ~30 m ASL, and corrected for the ship's heading and speed. Air temperature, relative humidity and solar radiation were measured on the monkey deck (the topmost accessible height) at a height of ~18.5 m ASL. Sea water temperature and chlorophyll in sea water were obtained from port side seawater intake at a depth of −5 m. The full list of parameters obtained during the voyages are detailed in Symons (2018a-c, 2019a-c).

2.2. *Meteorological reanalysis data*

The Modern-Era Retrospective analysis for Research and Applications, Version 2 (MERRA-2) is a meteorological reanalysis data product produced by the National Aeronautics and Space Administration Global Modeling and Assimilation Office (NASA/GMAO) (Gelaro et al., 2017). MERRA-2 data were extracted along the voyage tracks using spatial

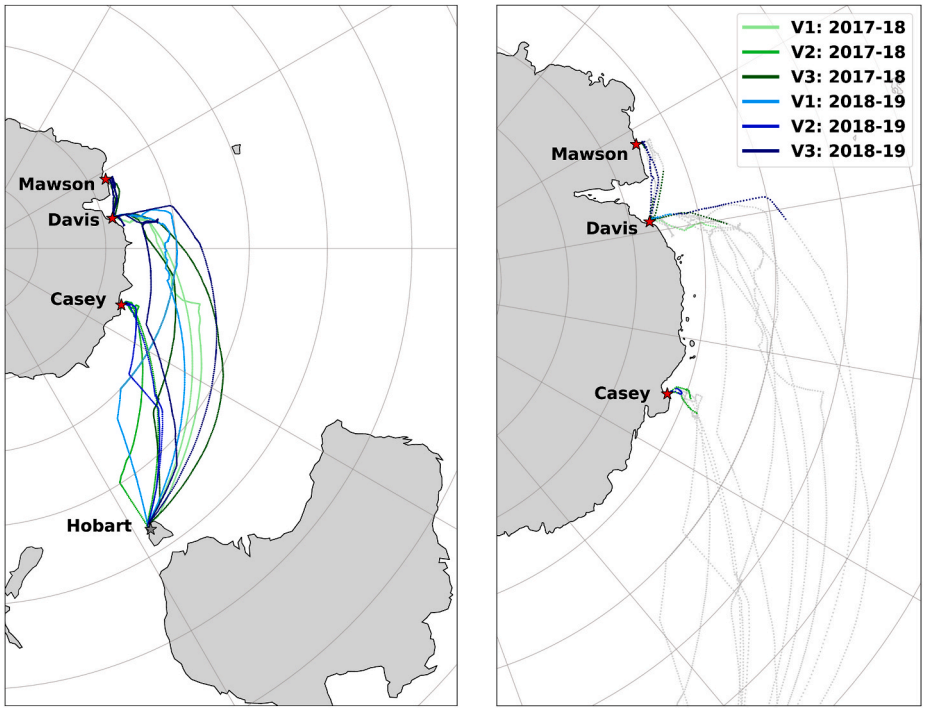

Fig. 1. Ship tracks for the CAMMPCAN voyages. The left panel shows the full tracks, coloured by voyage. The right panel shows a zoomed-in view, with the coloured points indicating the subset of data used for analysis (when the ship was docked on station or otherwise located within the sea ice). The locations of Mawson, Davis and Casey stations are also shown (red stars).

linear interpolation following the method described by Swanson et al. (2020). Potential temperature at altitudes of 2 m, 100 m and 1000 m were obtained using atmospheric pressure and temperature. The Richardson mixed layer height (MLH) was then calculated as the lowest altitude at which the value of the Bulk Richardson number (R_{ib}) reached a critical threshold (McGrath-Spangler and Molod, 2014; Seibert et al., 2000). A critical threshold of $R_{ib} > 0.25$ was used to match the threshold used by Swanson et al. (2020).

Several additional derived variables were calculated from the MERRA-2 reanalysis products using Equations (1)–(4). These included the change in pressure from one hour to the next (ΔP_{1hr}), the potential temperature differential in the lowest 1000 m ($\Delta\theta_{1000m}$) and the potential temperature differential in the lowest 100 m ($\Delta\theta_{100m}$):

$$Ri_b = \left(\frac{gz}{\theta_{v0}}\right)\left(\frac{\theta_{vz} - \theta_{v0}}{u_z^2 + v_z^2}\right) \quad (1)$$

$$\Delta P_{1hr} = P_t - P_{t-1} \quad (2)$$

$$\Delta\theta_{1000m} = (\theta_{1000m} - \theta_{2m}) \quad (3)$$

$$\Delta\theta_{100m} = (\theta_{100m} - \theta_{2m}) \quad (4)$$

where: g is the acceleration due to gravity (9.80665 m s^{-2}), z is the altitude (m), θ_{v0} is the virtual potential temperature at surface (K), θ_{vz} is the virtual potential temperature at altitude z (K), u_z is the eastward wind at height h (m s^{-1}), v_z is the northward wind at height h (m s^{-1}), P_t is the sea level pressure at time t (hPa), P_{t-1} is the sea level pressure at time $t–1$ hour (hPa), θ_{1000m} is the potential temperature at 1000 m altitude (K), θ_{100m} is the potential temperature at 100 m altitude (K) and θ_{2m} is the potential temperature at 2 m altitude (K).

2.3. Back trajectories

The HYbrid Single-Particle Lagrangian Integrated Trajectory (HYSPLIT) model (Draxler, 1999; Draxler and Hess, 1997, 1998; Stein et al., 2015) was used to calculate air mass back trajectories. Five-day (120-h) back trajectories were calculated by initialising HYSPLIT at 1-h intervals and at altitudes of 10 m, 100 m, 500 m and 2000 m from points corresponding to the ship's average latitude and longitude during each hour.

2.4. Sea ice data

Satellite observations of sea ice cover were acquired from the National Snow and Ice Data Center (NSIDC). We used the *NOAA/NSIDC Climate Data Record of Passive Microwave Sea Ice Concentration, Version 3* (Meier et al., 2017) for October 2017 to March 2019.

The air mass sea ice contact time was calculated by combining the HYSPLIT back trajectories with the sea ice cover observations and counting the number of hours that the air mass encountered sea ice, at 1-h time steps along each 5-day back trajectory. For this purpose, at each time step (1-h resolution), the latitude and longitude of the back trajectory was matched to the NSIDC sea ice data. Sea ice contact (designated by a value of one) was identified if the trajectory was located above the sea ice and below an altitude of 100 m ASL. The total sea ice contact time for each trajectory was then calculated as the sum of the hours for which sea ice contact occurred. This provides a measure of the amount of contact between air masses and the sea ice on a scale from 0 (no sea ice contact) to 120 h (constant sea ice contact throughout the five days). A similar methodology was used by Burgay et al. (2023) to identify ocean and sea ice origins of bromine species transported to the Antarctic Plateau.

3. Variable selection and data filtering

Our aim in this work is to probe the relationship between concentrations of BrO and Hg^0 and potential meteorological and environmental drivers. For this purpose, the observations of BrO and Hg^0 are treated as the dependent variables in this analysis. In this section, we detail the selection of meteorological and environmental variables for our analysis as well as the data filtering methods employed. All datasets were re-averaged to a standard temporal resolution of 1 h prior to analysis. The number of hourly BrO and Hg^0 observations from each voyage are detailed in Table S2.

We considered a total of 15 potential explanatory variables. These included nine variables identified as important drivers for Arctic BrO (Swanson et al., 2020): surface O_3, AEC, surface temperature, sea level pressure, hourly rate of change in surface pressure, wind speed, MLH and potential temperature differentials ($\Delta\theta_{1000m}$, $\Delta\theta_{100m}$). We also considered six additional variables that have previously been shown to be associated with BrO abundance: relative humidity (Hara et al., 2020; Huang and Jaeglé, 2017; Pöhler et al., 2010), sea surface temperature (Henley et al., 2017), solar radiation levels (Prados-Roman et al., 2018), sea ice cover (Peterson et al., 2019), chlorophyll concentration in surface waters (Abrahamsson et al., 2018; Hughes et al., 2013), and air mass sea ice contact time (Bognar et al., 2020; Frieß et al., 2023; Wagh et al., 2023). Further rationale for the choice of variables can be found in Section S1 of the supplement.

All potential variables were tested for normality using the Shapiro-Wilk test (Shapiro and Wilk, 1965). The hourly observations of BrO and AEC were found to have non-Gaussian distributions. The BrO and AEC datasets were therefore square root and log transformed, respectively, to approximate near-Gaussian distributions, following Swanson et al. (2020). We then performed regression analysis between the transformed BrO observations and the different potential environment drivers (including both the variables used by Swanson et al., 2020 for the Arctic and the additional variables described above).

Table 1 shows the results of the regression analysis, including the correlation coefficient (R) and percent of BrO variance explained by each environmental variable. Ten of the variables were significantly correlated with BrO_{surf} and 14 with BrO_{LTcol}. This suggests that changes in these variables are correlated with changes in BrO, and therefore merit inclusion in further analysis. Of the correlated variables, relative humidity, water temperature, solar radiation and sea ice cover individually explained the largest proportion of variability in BrO_{LTcol} (6.5–12%). None of these four variables had been included in the Arctic model developed by Swanson et al. (2020). Note that of the nine environmental variables used by Swanson et al. (2020) (marked (i) in Table 1), only four (O_3, surface temperature, wind speed and $\Delta\theta_{100m}$) were found to be statistically significantly correlated with BrO_{surf}; however, all variables except ΔP_{1hr} were significantly correlated with BrO_{LTcol}. The lower percent of variance explained for BrO_{surf} than for BrO_{LTcol} may reflect limitations of both the BrO dataset and the set of environmental variables included our analysis, as will be discussed in Section 4.4 following further statistical analysis.

The 14 variables with significant correlation with BrO were tested for multicollinearity by calculating variance inflation factors (VIFs). None of the variables were determined to have a critical degree of multicollinearity, defined as VIF >5 (Rogerson, 2001). As a result, the first 14 variables shown in Table 1 were used to develop predictive models for BrO. All 14 variables were standardised by subtracting the mean and dividing by the standard deviation so that variables with unequal variance could be included in the analysis.

Following selection and standardisation of the variables, the hourly dataset was filtered for completeness (all variables available for the hour). The data was then filtered to meet conditions that are conducive to reactive bromine events, following Swanson et al. (2020), based on observation date, ozone concentration, and pollution as described in Section S2 of the supplement. After applying all filters, our final dataset included 695 hourly data points (Table S3).

Table 1
Correlation and percent of variance explained for regression of environmental variables against square-root-transformed BrO_{LTcol} and BrO_{surf}. Correlations are statistically significant at $p < 0.05$ unless listed as *n.s.* (not significant).

Variable	$\sqrt{(BrO_{LTcol})}$			$\sqrt{(BrO_{surf})}$		
	Rank	*R*	Variance explained	Rank	*R*	Variance explained
Relative humidity - RH (%)	**1**	−0.347	12.06%	4	−0.202	4.09%
Water temperature - T_w (°C)	**2**	−0.322	10.38%	1	−0.277	7.66%
Solar radiation - SR (W/m^2)	**3**	0.314	9.84%	10	0.086	0.73%
Sea ice cover - f_{ice} (%)	**4**	−0.254	6.46%	6	−0.139	1.93%
O_3 (ppb)[i]	**5**	0.253	6.40%	3	0.224	5.02%
Wind speed at 10 m - ν (m/s)[i]	**6**	−0.238	5.66%	7	−0.114	1.30%
$\Delta\theta^{i}_{100m}$	**7**	−0.235	5.52%	8	−0.103	1.05%
log(AEC)[i]	**8**	−0.214	4.59%	13	*n.s.*	*n.s.*
Surface temperature - T_s (C)[i]	**9**	−0.195	3.81%	2	−0.247	6.08%
Chlorophyll in sea water - Chl (μg/l)	**10**	−0.171	2.93%	11	*n.s.*	*n.s.*
MLH (m)[i]	**11**	0.157	2.47%	16	*n.s.*	*n.s.*
Surface pressure - P_s (hPa)[i]	**12**	0.119	1.41%	12	*n.s.*	*n.s.*
Ice contact time - t_{ice} (hours)	**13**	−0.099	0.97%	5	−0.145	2.10%
$\Delta\theta^{i}_{1000m}$	**14**	−0.088	0.78%	15	*n.s.*	*n.s.*
P_{1hr} (hPa)[i, ii]	**15**	*n.s.*	*n.s.*	14	*n.s.*	*n.s.*

Notes: (i) Variables used by Swanson et al. (2020); (ii) Variables not included in the predictive model.

4. Results and discussion

4.1. Dataset characterisation

The means and range (within one standard deviation) for each variable considered for this analysis are shown in Table 2 and where relevant compared to the Arctic equivalents reported by Swanson et al. (2020). Mean BrO_{surf} and BrO_{LTcol} concentrations for the Antarctic (2.0×10^{12} and 10.3×10^{12} molecules cm^{-2}, respectively) were lower than those observed by Swanson et al. (2020) for the Arctic (4.2×10^{12} and 13.4×10^{12} molecules cm^{-2}, respectively). This is likely because the Arctic observations start from polar sunrise (21 February) in early spring, when temperatures are colder and BrO concentrations are at their highest (Pöhler et al., 2010; Simpson et al., 2018). In contrast, the Antarctic BrO observations used here were collected during short ship-based campaigns that took place during the warmer late spring (7 Nov) through late summer (21 Feb) seasons. Mean observed temperature during CAMMPCAN was -2.1 ± 3.1 °C, approximately 12 °C warmer than the mean Arctic surface temperature of −14.2 °C reported by Swanson et al. (2020). With a lack of observations around polar sunrise, direct comparisons with the Arctic dataset are difficult. The CAMMPCAN Antarctic dataset is unlikely to capture the full range of BrO concentrations due to the lack of early spring data, although elevated BrO amounts have also been observed in summer and autumn in the coastal Antarctic (Frieß et al., 2023).

The mean potential temperature differentials derived from MERRA-2 for the lowest 1000 m ($\Delta\theta_{1000m}$) and 100 m ($\Delta\theta_{100m}$) were 3.0 K and −0.2 K, respectively, indicating that on average the Antarctic lower troposphere was stable and the surface layer was very slightly unstable. Of the 694 points in the dataset, 533 indicated a stable surface layer (positive $\Delta\theta_{100m}$) and 661 indicated a stable lower troposphere (positive $\Delta\theta_{1000m}$). The minimum $\Delta\theta$ were −1.3 K and −0.9 K for the lowest 100 m and 1000 m, respectively. Temperature inversions are a common feature of coastal Antarctica, and in comparison, to the Arctic, they occur much more frequently during the summer months (Nygård et al., 2013). Inversions are particularly common during late spring when open leads start to form in the coastal sea ice. Open leads expose relatively warm water temperatures to cooler air temperatures above. This can result in convective mixing, causing negative $\Delta\theta$ and an unstable atmosphere (Moore et al., 2014).

BrO_{surf} partial columns decreased between spring and summer (V1 to V3, Table S2), likely resulting from the seasonal reduction in sea ice cover. The seasonal BrO_{surf} decrease at Davis (the only station visited in both seasons) is shown in Fig. 2. As shown in Fig. 3, the observations indicate a positive relationship between BrO_{surf} partial columns and sea ice cover during periods of both low wind speeds (<7 m s^{-1}) and high wind speeds (>7 m s^{-1}). Jones et al. (2009) proposed two regimes for enhanced BrO in sea ice regions as an outcome of changes in wind speed. Low wind speeds combined with strong atmospheric stability above the snowpack can allow photolabile bromine species to accumulate in the boundary layer and subsequently react with O_3 to form BrO (Peterson et al., 2015). Meanwhile, high wind speeds (>7 m s^{-1}) can result in the lofting of sea salt aerosols from the sea ice surface that provide a surface for heterogenous chemistry (Hara et al., 2020), resulting in the release of Br_2 that subsequently reacts with O_3 to form BrO (Jones et al., 2009). Potential sources for these sea salt aerosols during high wind speed conditions include sublimation of blowing snow (Frey et al., 2020; Giordano et al., 2018; Lieb-Lappen and Obbard, 2015) or dispersion from sea ice (Hara et al., 2020). The CAMMPCAN dataset supports BrO formation under both low and high wind speed regimes. Additional factors that drive the distribution of BrO over coastal Antarctica will be investigated below.

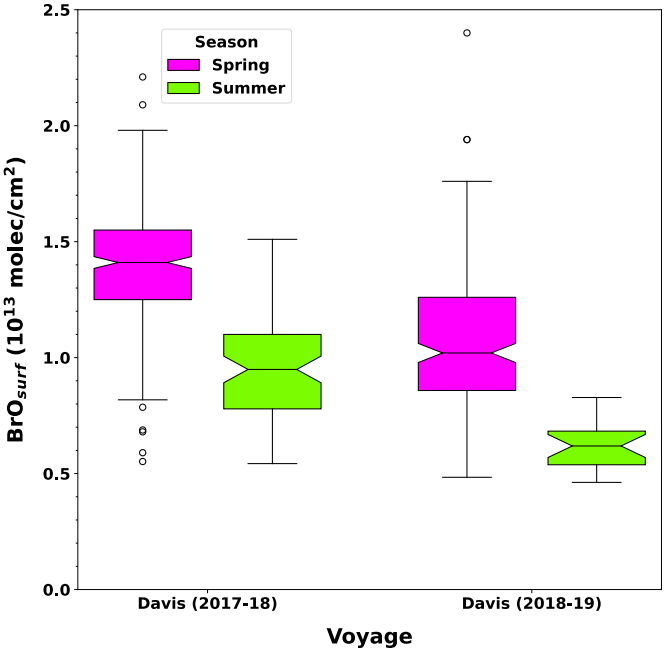

Fig. 2. Seasonal distribution of BrO_{surf} partial columns at Davis in spring (V1, pink) and summer (V3, green). 'Spring' refers to 14–23 Nov for the 2017-18 campaign and 7–16 Nov for the 2018-19 campaign. 'Summer' refers to 27–30 Jan and 19–21 Feb for the 2017-18 campaign and 26–28 Jan and 19–20 Feb for the 2018-19 campaign.

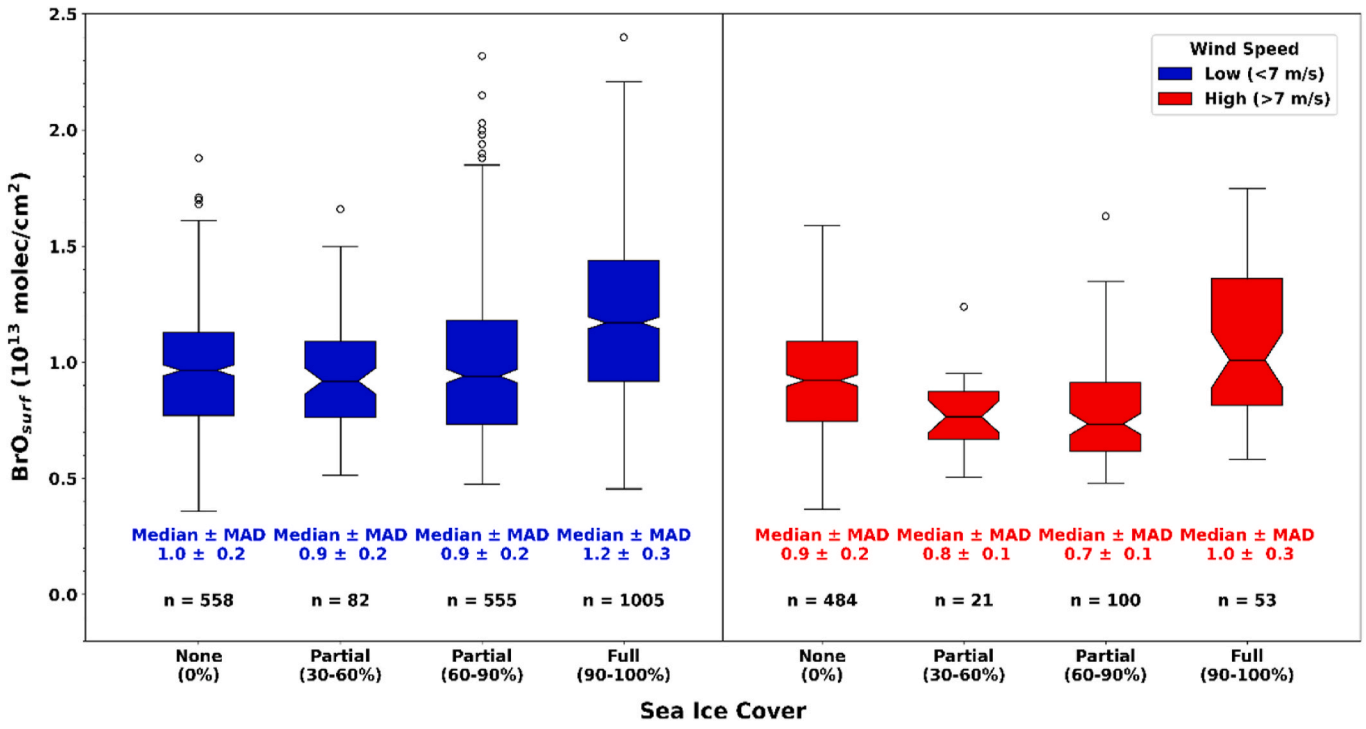

Fig. 3. BrO_{surf} partial columns binned by wind speed (colors) and sea ice cover (x-axis) for periods when the Aurora Australis was anchored on station. The median ± median absolute deviation (MAD) and number of observations in each bin (n) are also indicated.

4.2. Evaluation of the arctic predictive model

Before developing an Antarctic-specific model for BrO prediction, we first evaluated whether the predictive model previously developed for the Arctic by Swanson et al. (2020) was applicable to the CAMMPCAN dataset. The Arctic model included nine environmental variables (see Table 2), including some that did not correlate strongly to Antarctic BrO observed during CAMMPCAN and excluding others that we found to correlate strongly with Antarctic BrO (see Section 3).

The Swanson et al. (2020) Arctic predictive model was found to perform poorly in the Antarctic, overestimating BrO concentrations and failing to accurately reproduce the variability as shown in Figs. S2 and S3. The squared correlation coefficient between predictions and observations was $R^2 = 0.031$ for BrO_{surf} and $R^2 = 0.0069$ for BrO_{LTcol}, implying the Arctic model could explain less than 10% of the variability in either BrO partial column observed in Antarctica. This finding, combined with the correlation analysis presented in Section 3, suggests that environmental factors not included in the Swanson et al. (2020) model may be important drivers of Antarctic BrO variability. These results hint at key differences between the Arctic and Antarctic in the factors that drive BrO variability and motivated us to develop a new Antarctic-specific predictive model. We also expect an Antarctic-specific model to be necessary for interpreting mercury observations (Section 4.5), given the known differences between Arctic and Antarctic mercury cycling and the poor performance of empirical mercury models in the Antarctic (Angot et al., 2016a).

4.3. Statistical modes of Antarctic variability

To develop a predictive model for Antarctic BrO, we followed the method of Swanson et al. (2020) by first using principal component analysis (PCA) to identify the dominant modes of environmental variability in the Antarctic (PCs) (this section), and then regressing the identified PCs against observed BrO (Section 4.4). PCA is a statistical procedure for computing the principal components that explain the variance within a dataset by identifying patterns among several variables (Mardia et al., 1979). Here, we used as inputs to the PCA the 14 environmental variables identified in Section 3, transformed, standardised to equal variance, and filtered as described in Section S2, resulting in 14 PCs. Note that this step is independent of BrO. Backward stepwise selection was used to systematically remove the least

Table 2
Mean (μ) and range of values within one standard deviation of the mean (μ-σ, μ+σ) of BrO partial columns, Hg^0 concentrations, and explanatory variables from CAMMPCAN and, where relevant, Swanson et al. (2020).

Variable	CAMMPCAN (Antarctic)			Swanson et al. (2020)[i] (Arctic)		
	μ - σ	μ	μ + σ	μ - σ	μ	μ + σ
BrO_{LTcol} (10^{12} molec cm^{-2})[ii]	7.3	10.3	13.4	3.9	13.4	28.6
BrO_{surf} (10^{12} molec cm^{-2})[ii]	1.4	2.0	2.5	1.2	4.2	9.3
Hg^0 (ng m^{-3})	0.32	0.50	0.68	–	–	–
O_3 (ppb)	12	17	21	8	21	33
Sea level pressure (hPa)	977	983	990	1011	1020	1029
Surface temperature (°C)	−5.2	−2.1	1.1	−22.0	−14.2	−6.4
$\Delta\theta_{1000m}$ (K)	1.3	3.0	4.7	6.5	11.5	16.5
$\Delta\theta_{100m}$ (K)	−0.7	−0.2	0.2	−0.6	0.3	1.1
Wind speed at 10 m (m s^{-1})	1.4	5.2	9.1	2.8	5.6	8.3
MLH (m)	343	605	866	160	330	500
Solar radiation (W m^{-2})	216.8	462.5	708.1	–	–	–
Ice contact time (hours)	−5.2	22.3	49.7	–	–	–
Sea ice cover (%)	10	38	66	–	–	–
Chlorophyll in sea water (μg L^{-1})	−1	3	8	–	–	–
Water temperature (°C)	−1.7	−1.1	−0.6	–	–	–
Relative humidity (%)	47.4	61.7	76.0	–	–	–
AEC lowest 200 m (km^{-1})[ii]	0.001	0.011	0.171	0.014	0.060	0.256

Notes: (i) Variables not reported by Swanson et al. (2020) indicated by "-". (ii) Values for BrO and AEC were calculated from transformed values (see Section 3) then converted back to non-transformed values for this table.

significant principal components and test the impact on the R^2 of the statistical model for BrO (described in the next section). Based on this analysis, we retained the first three PCs, which collectively explained 26% of the overall variability in BrO and each individually added at least 0.02 to the overall R^2 (i.e., 2% to the variability explained) (Fig. S4).

Fig. 4 shows the loadings for the first three PCs (referred to here as PC1, PC2, and PC3), with full details available in Table S4. PC1 consists mainly of high O_3 and a thick mixed layer (high MLH), combined with reduced sea ice cover, cold surface temperatures, decreased stability in the lowest 100 m and 1000 m and somewhat decreased surface pressure. PC1 has minimal dependence on surface wind speeds, sea ice contact time, or aerosol extinction. These are the same characteristics as PC1 from the Arctic PCA (Swanson et al., 2020), which described conditions with an unstable atmosphere and increased vertical mixing caused by low-pressure systems. The highest loadings in the modified PC1 found here are similarly consistent with a vertical mixing mode associated with an unstable atmosphere and driven by Antarctic low-pressure systems. Antarctica is typically surrounded by a belt of low-pressure systems known as the circumpolar trough, and the occurrence of low-pressure systems is a common feature of Antarctic coastal areas (Jones et al., 2010; Schlosser et al., 2011). The high O_3 concentrations suggest this mode could also be associated with the katabatic winds that are a well-known feature of coastal East Antarctica (Angot et al., 2016b). These winds can form a trapping layer, confining emissions near the surface, leading to potential high-NO conditions (Slusher et al., 2010) and enhanced O_3 production (Helmig et al., 2008).

PC2 consists mainly of increased sea ice contact time, high surface wind speed, high relative humidity and increased aerosol extinction, combined with decreased surface pressure, decreased solar radiation and decreased surface stability in the lowest 1000 m. PC2 has minimal influence from surface stability in the lowest 100 m or chlorophyll in surface waters. PC2 indicates negative loadings for surface temperature and potential temperature differential in the lowest 100 m and positive loadings for surface wind speed, mixed layer heights and aerosol extinction. This mode is consistent with a blowing snow mechanism whereby increased surface wind speeds drive the vertical mixing of saline snow particles on sea ice, leading to a deeper mixed layer with increased aerosol extinction and the reduced incidence of solar radiation (Jones et al., 2009; Yang et al., 2019). While this mode has some similarity to PC1 and to the Arctic mixing mode (PC1) identified by Swanson et al. (2020), the additional information provided by the sea ice contact time provides a unique link to the role of blowing snow.

PC3 consists mainly of high surface wind speed, high chlorophyll concentration in surface waters and a thick mixed layer, combined with limited sea ice contact time, low relative humidity, and low O_3. PC3 has minimal dependence on surface pressure, surface temperature, sea ice cover, or aerosol extinction. Sea ice contact has a negative loading in PC3, suggesting that this mode is stronger in the absence of sea ice and therefore has increased importance during the summer months. This mode is consistent with an oceanic source, with high wind speeds driving vertical mixing of compounds emitted from the ocean. The high chlorophyll loading in PC3 could imply a role for biological activity.

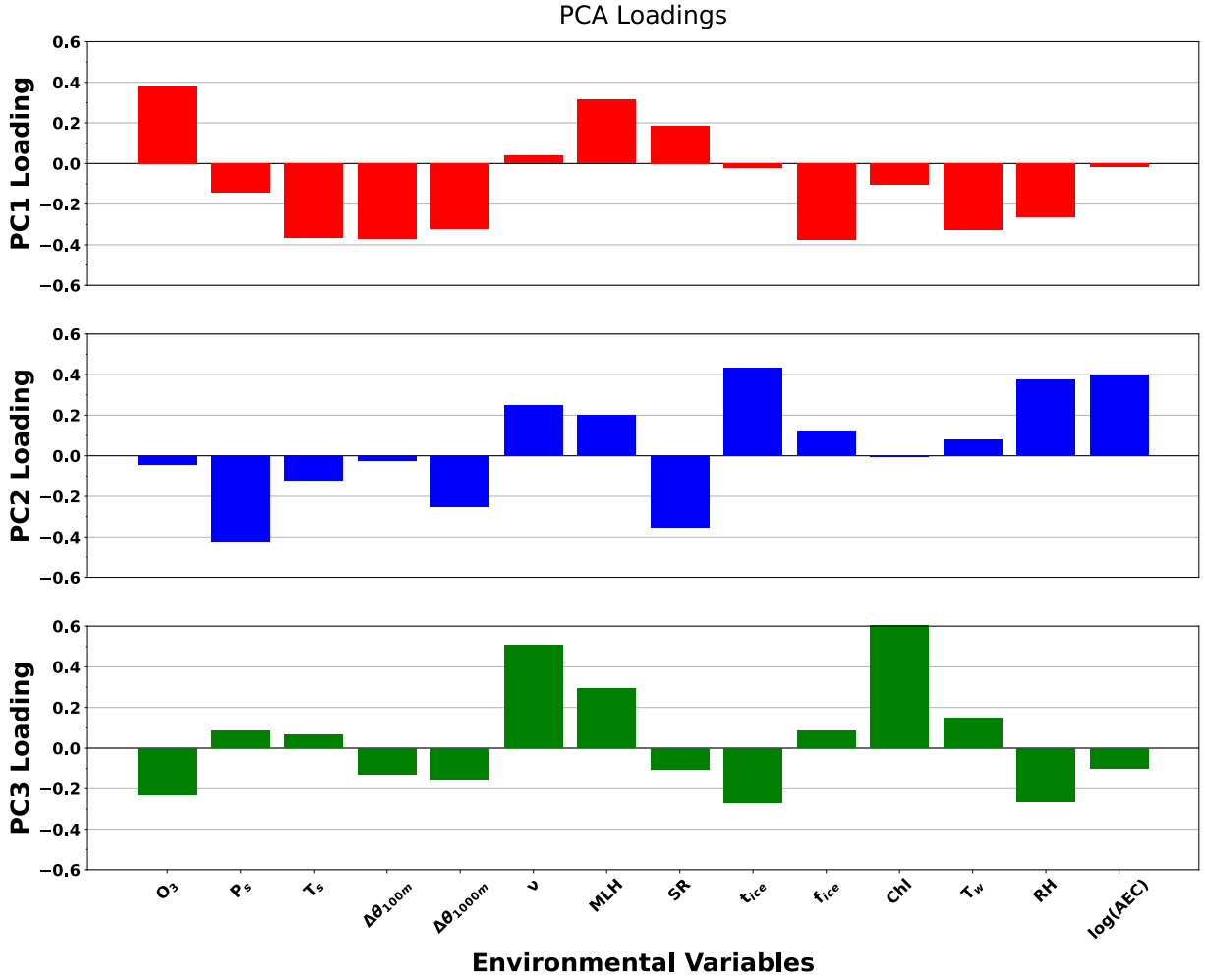

Fig. 4. Loadings of the first three principal components from the Antarctic PCA. Each bar represents the weight assigned to a given variable for a given principal component. See Table 1 for variable definitions.

Seasonal phytoplankton blooms are common across large areas of the Southern Ocean, particularly in coastal areas and close to the edge of sea ice, leading previous studies to speculate that oceanic emissions of organic bromine could be important for the chemistry of the Antarctic troposphere (Hughes et al., 2009, 2012). Alternatively, PC3 could represent an inorganic ocean source, with enhanced BrO at other Antarctic sites previously attributed to sea salt aerosols (Frieß et al., 2023). However, PC3 shows limited (and slightly negative) dependence on aerosol extinction, in contrast to the strong positive correlation Frieß et al. (2023) associated with a sea salt source. Distinguishing between these mechanisms (ocean biological activity versus sea salt aerosols) is not possible with the CAMMPCAN dataset but could be attempted in future campaigns with halocarbon and/or sea salt aerosol observations. The general characteristics of PC3 do not appear related to any of the PCs identified in the Arctic by Swanson et al. (2020), suggesting that PC3 describes a mode that plays a more important role in the Antarctic than in the Arctic.

4.4. Predictive model for Antarctic BrO

We used ordinary least squares linear regression to fit the timeseries of observed BrO partial columns to the three dominant PCs using principal component regression (PCR). The outcome of this process yields equations to predict standardised values of the dependent species (here, BrO partial columns) based on timeseries combinations of each PC multiplied by an empirically derived coefficient. For BrO_{surf}, we found that the PCR could not reproduce the observed variability ($R = 0.40$; $R^2 = 0.16$). This result likely reflects the vertical distribution of Antarctic BrO, as the BrO vertical profile retrievals from the CAMMPCAN data show that the BrO maximum rarely resides in the surface layer. The poor model performance for BrO_{surf} may also indicate that important environmental variables were missing from our analysis. Given the PCR was unable to reproduce the observed variability, we dropped BrO_{surf} from further analysis.

For BrO_{LTcol}, the PCR showed more skill. The fit coefficients are given in Equation (5):

$$BrO_{LTcol} = \left(3.19{\cdot}10^{6} + \left(8.47{\cdot}10^{4} \times PC1\right) + \left(-1.24{\cdot}10^{5} \times PC2\right) + \left(-4.27{\cdot}10^{4} \times PC3\right)\right)^{2} \quad (5)$$

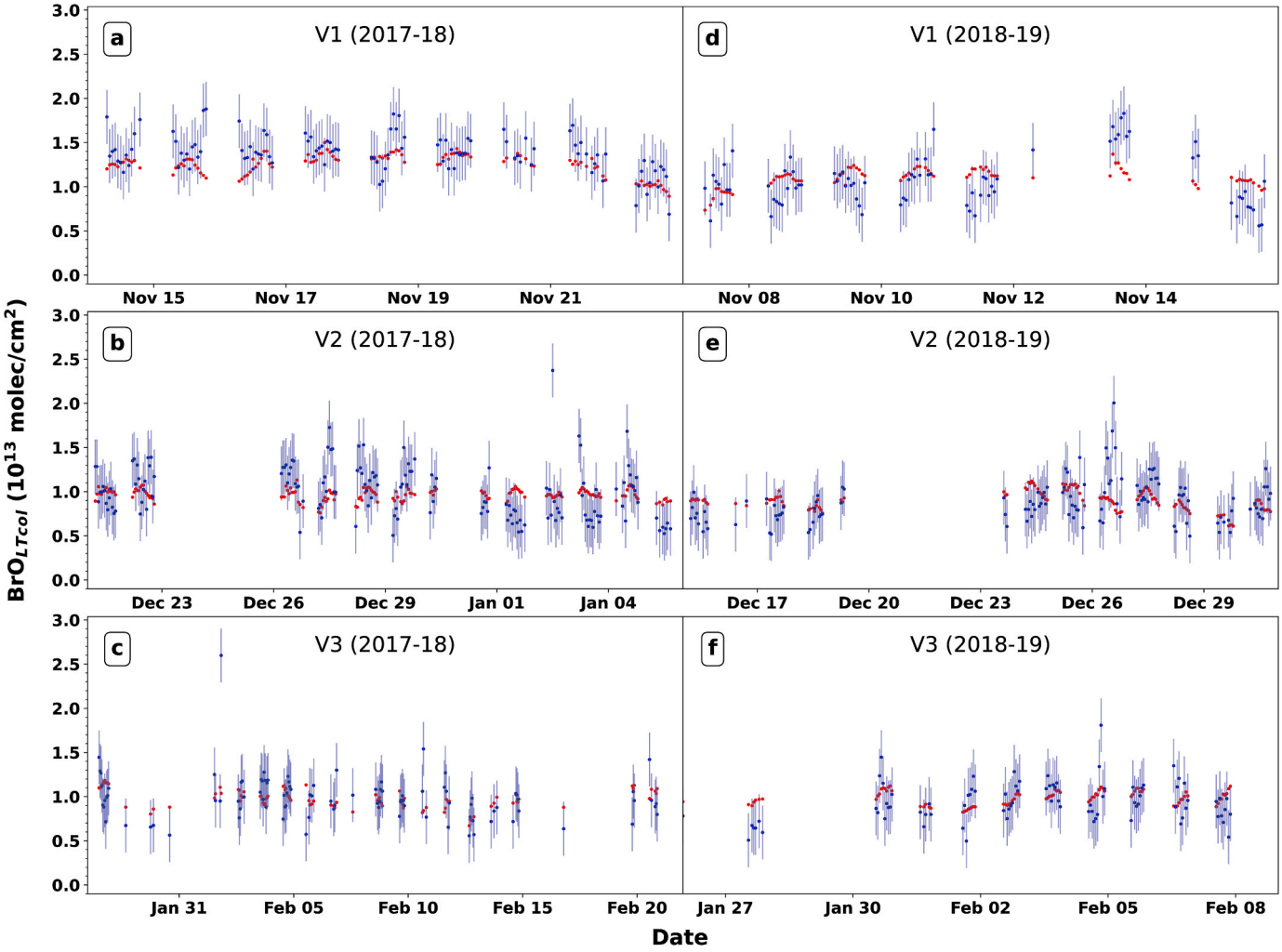

Fig. 5. Timeseries of predicted (red) and observed (blue) BrO_{LTcol} from the 2017–18 (a: V1, b: V2, c: V3) and 2018–19 (d: V1, e: V2, f:V3) CAMMPCAN voyages. Observations are shown as the hourly means (dots) ± one standard deviation (error bars). Overall, the comparison results in $R^2 = 0.26$, mean normalised bias of 4.8% and mean normalised error of 21.0%. Statistics for each campaign can be found in Table S5.

Fig. 5 shows the timeseries of BrO_{LTcol} predictions from the Antarctic PCR model along with MAX-DOAS observations of BrO_{LTcol}. Statistical comparisons between the predictions and the observations are detailed in Table S5. The R^2 between the BrO_{LTcol} predictions and observations implies that the new PCR model explains 26% of the variability ($R = 0.51$; $R^2 = 0.26$), compared to only 0.7% ($R = 0.08$; $R^2 = 0.007$) when using the Arctic PCR model derived by Swanson et al. (2020). This represents a substantial improvement in predictive capability relative to the Arctic-based model. The mean normalised bias of the predictions is 4.8% (~5.0×10^{11} molecules cm^{-2}) of the observed mean. The Antarctic PCR model performs better in 2017–18 than in 2018–19, describing 30.7% and 11.2% of the variability during these campaigns, respectively. For the individual voyages, the model performs best for V1 in 2017–18 (15.0% variability explained) followed by V3 in 2018–19 (7.8% variability explained).

Fig. 5 shows that the BrO_{LTcol} predictions are usually within one standard deviation of the observed BrO_{LTcol}. However, the diurnal cycle of the predictions does not always align with the diurnal cycle of the observations. Potential reasons for this discrepancy include: (i) the MERRA-2 values used for the mixed layer height and potential temperature differentials could be inaccurate for local conditions (MERRA-2 grid cell size is 0.5° latitude x 0.625° longitude) or (ii) there may be other environmental drivers that are not included in the model but contribute to the true variability of Antarctic BrO_{LTcol}. For example, the inclusion of land and ocean contact time variables might have helped to separate coastal/oceanic airmasses from the continental airmasses (Frieß et al., 2023), although this would have created issues with multicollinearity with the ice contact time variable. An alternative method for separating air masses into oceanic, coastal and continental origins that could be explored in future would be to use radon observations (Chambers et al., 2017).

Fig. 6 shows the variability of each PC coincident with variability in the overall prediction of BrO_{LTcol} from the PCR. Recall that PC1 describes a vertical mixing mode with elevated O_3, which provides the conditions to lift bromine-rich air from the surface that can produce BrO in the lower troposphere. PC1 had the highest values during V1 in both 2017–18 (Fig. 6a) and 2018–19 (Fig. 6d), suggesting that the mixing mode was most important as a driver of Antarctic BrO concentrations during spring. Note that PC1 had a negative value during V2 in both 2017–18 (Fig. 6b) and 2018–19 (Fig. 6e). This could indicate the presence of high-pressure systems, causing lower BrO concentrations across the lower troposphere through a lack of vertical mixing. The vertical profiles of BrO indicate that the highest BrO concentrations are typically found at an altitude of 300–500 m ASL, rather than in the surface layer

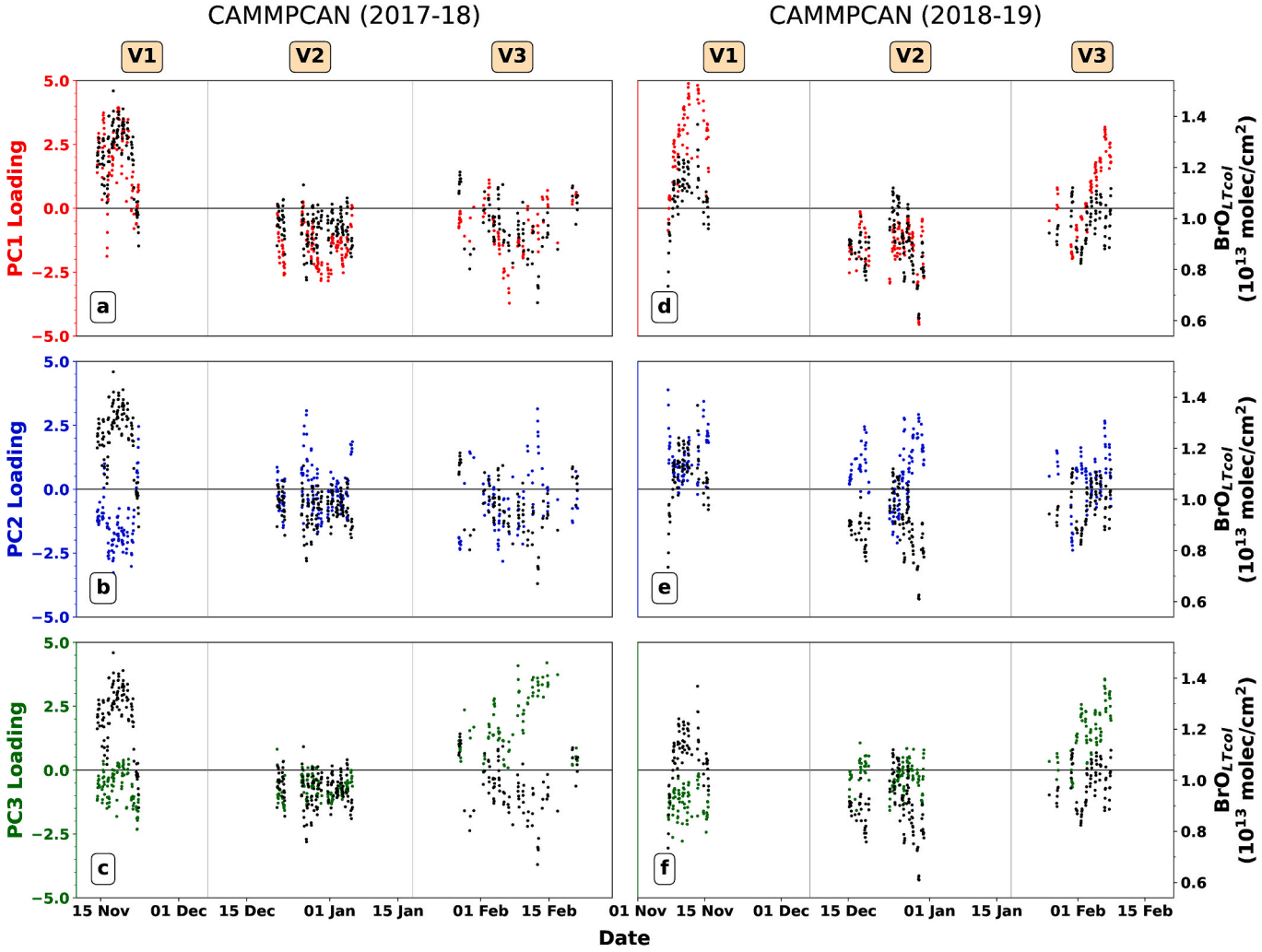

Fig. 6. Values of PC1, PC2 and PC3 (colors, left y-axis) along with predictions of BrO_{LTcol} (black, right y-axis) from the Antarctic PCR model during the CAMMPCAN 2017–18 (left) and 2018–19 (right) voyages. (a, d) PC1 loading (red), (b, e) PC2 loading (blue) and (c, f) PC3 loading (green) are the sum of each standardised variable multiplied by its respective loading (see Table S5). The black horizontal line shows PC = 0 along with the mean observed BrO_{LTcol} concentration across all voyages (1.04×10^{13} molec cm^{-2}).

(<200 m) (not shown). This suggests that elevated BrO concentrations are typically associated with increased vertical mixing, consistent with the coincidence between elevated BrO_{LTcol} and elevated PC1. Hay (2011) similarly reported enhanced BrO at McMurdo Sound in conjunction with low-pressure systems.

As described in Section 4.3, blowing snow, as identified by PC2, promotes the formation of BrO through heterogenous reactions on aerosols. PC2 had the highest values during V1 and V2 in 2018–19 (Fig. 6d and e), suggesting that the blowing snow mode was active during springtime and early summer in this year. PC2 had a negative contribution during V1 in 2017–18 coincident with elevated BrO (Fig. 6a), which could suggest that the elevated BrO at that time was not associated with the blowing snow mechanism. Jones et al. (2009) described another mechanism for enhanced BrO, whereby calm surface conditions allow for Br_2 to accumulate above the snowpack and then be converted BrO. It is possible that this mechanism was more active than the blowing snow mechanism during V1 2017–18.

An ocean source, as identified by PC3, could enhance the production of BrO from organic bromocarbons and/or sea salt aerosol. The low values for PC3 during V1 in 2017–18 (Fig. 6a) and 2018–19 (Fig. 6d) imply that the ocean source had little impact during springtime when sea ice cover was high. In contrast, PC3 had the highest values during V3 in both 2017–18 (Fig. 6c) and 2018–19 (Fig. 6f), implying that the ocean source of BrO was most important during the summer months. The absence of sea ice in summer is associated with more time over the open ocean, enabling more air mass contact time with bromocarbon emissions (Hossaini et al., 2013) and/or sea salt aerosol (Frieβ et al., 2023). Previous studies have shown that bromocarbons can form localised hotspots where emissions to the atmosphere are relatively strong (Hossaini et al., 2013). For example, between 2005 and 2007, bromocarbon hotspots on the Antarctic Peninsula were found to result from annual phytoplankton blooms that coincided with the break-up of sea ice during the summer months (Dec–Feb) (Hughes et al., 2009). In addition, algae/phytoplankton are more active at this time of year due to increased sunlight, which could enhance photosynthetic activity. Alternatively, reactive bromine release from ocean-derived aerosols could explain the relationship with PC3. Using simple linear regression at Neuymayer and Arrival Heights, Frieβ et al. (2023) found strong correlations between BrO and aerosol extinction, as well as between BrO and open water contact time, particularly at the strongly ocean-influenced Neumayer site. They attributed these correlations to a sea spray and/or sea salt aerosol source in summer. Here, we find that PC3 is not associated with high aerosol extinction (in fact, the aerosol extinction loading for PC3 is somewhat negative), which implies sea salt aerosol is less likely to be the sole driver of the BrO-PC3 relationship. However, without halocarbon and aerosol sampler sea-spray observations, it is not possible to distinguish between organic and inorganic sources of BrO associated with PC3 in the CAMMPCAN dataset.

Although the three principal components are statistically independent, the three processes identified above work concurrently to influence BrO concentrations. During V1 2018–19 (Fig. 6d), both PC1 and PC2 were elevated. This combination suggests a low-pressure system, combined with cold temperatures, high wind speeds and increased sea ice contact. These conditions are conducive to enhanced BrO that originates from blowing snow events above the sea ice that are then mixed through the lower troposphere by low-pressure systems. These events are a common occurrence during springtime in the Antarctic (Jones et al., 2009; Prados-Roman et al., 2018). During V3 2018–19 (Fig. 6f), both PC1 and PC3 were elevated. This combination suggests that the BrO originated from an ocean source and was then mixed through the lower troposphere by a low-pressure system. Under these conditions, ocean waters rich in bromocarbons and/or sea salt aerosols would provide a source to the lower atmosphere, leading to enhanced BrO concentrations in the lower troposphere (Frieβ et al., 2023; Hughes et al., 2013).

4.5. Application to prediction of Hg^0

Variability in Antarctic BrO has implications for variability in Hg^0, a species of critical interest in polar regions due to the vulnerability of polar ecosystems to mercury bioaccumulation. However, we find that in the CAMMPCAN dataset, BrO partial columns explain less than 10% of observed variability in Hg^0 (6% for BrO_{surf}; 8% for BrO_{LTcol}). This result could indicate that BrO is in excess relative to Hg^0, in which case it would not be a limiting agent for Hg^0 oxidation and would not be a primary driver of Hg^0 variability. We therefore expect the environmental modes of Antarctic variability identified using the PCA may provide a more useful predictor of Hg^0 variability.

We applied the same data and methodology to Hg^0 as used for BrO, including using the same data selection, preparation and filtering. While Hg^0 observations are available at all hours (including in the dark), the use of AEC measured via MAX-DOAS as a predictor variable restricts the Hg^0 analysis to daytime hours when the sun is above the horizon (i.e., the same hours used for BrO). As for BrO, Hg^0 was found to have a non-Gaussian distribution and was therefore square root transformed to approximate a near-Gaussian distribution. Following the same methodology used for BrO (Section 3), we performed single linear regression analysis against all environmental variables. We found the 14 variables included in the PCA were all statistically significantly correlated with Hg^0 (Table S6), confirming the relevance for Hg^0 of the environmental variables underlying the PCA. The strongest correlation was with relative humidity ($R = 0.58$), a relationship that has previously been attributed to release of mercury from the snowpack during surface snow sublimation in summer (Cairns et al., 2021).

We also found a strong anti-correlation with land contact time (a variable we did not include in the PCA due to multicollinearity with ice contact time), explaining about 22.1% of the variability in Hg^0. We attribute this correlation to the influence of the Antarctic plateau. During summer, air masses over the Antarctic plateau are generally depleted in Hg^0 due to enhanced concentrations of oxidants (OH and NO_x) within the boundary layer (Kukui et al., 2014; Song et al., 2018). The high oxidant concentrations result from the UV photolysis of the nitrate anion (NO_{3-}) in snow grains, leading to emissions of NO_x from the snowpack (Angot et al., 2016b). Although this reactivity occurs predominantly over the Antarctic plateau, it is thought to influence Hg cycling in coastal areas during periods of katabatic airflow (Angot et al., 2016b). Observations by Unagar et al. (2021) indicate that periods of elevated Hg^0 concentrations coincide with shallow coastal air masses, while reduced Hg^0 concentrations typically coincide with air masses descending from the free troposphere or from deeper in the continent. Despite this correlation, for our analysis, we chose not to revise the PCA to include land contact time to avoid issues of critical multicollinearity and maintain consistency with BrO, for which ice contact time was a stronger predictor.

The PCR for Hg^0 resulted in the fit coefficients given in Equation (6):

$$Hg^0 = (0.698 + (-0.028 \times PC1) + (0.009 \times PC2) + (-0.044 \times PC3))^2 \quad (6)$$

Fig. 7 shows a timeseries of Hg^0 predictions using the PCR model along with hourly-averaged Hg^0 observations from the Tekran® 2537 A. The R^2 value between the Hg^0 predictions and observations suggests that the Antarctic PCR explains ~48% of the variability in Hg^0 ($R = 0.69$; $R^2 = 0.48$). This is higher than the variance explained for BrO_{LTcol} (~27%) and indicates a stronger relationship of the environmental variables with Hg^0 than with BrO_{LTcol} in the region. Statistical comparisons can be found in Table S7. The mean normalised bias of the Hg^0 predictions is 6.4% (~0.03 ng m^{-3}), and the predictions are generally within one standard deviation of the observed means. However, the Antarctic PCR fails to predict the magnitude of Hg^0 concentrations during periods of large Hg^0 enhancements. For example, on the December 29, 2018 (Fig. 7e), the Antarctic PCR model predicts enhanced Hg^0 (up to 0.83 ng

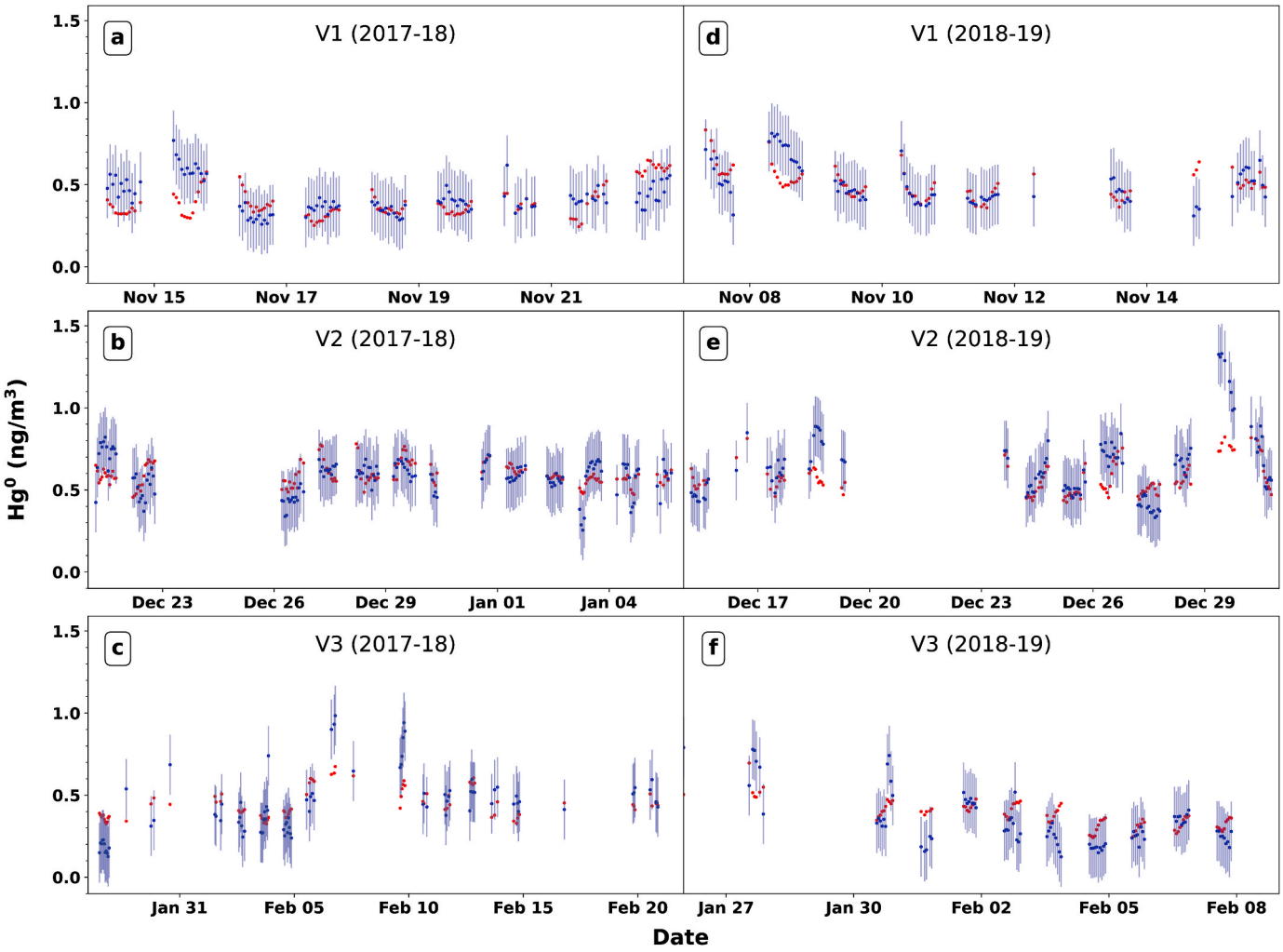

Fig. 7. Timeseries of predicted (red) and observed (blue) Hg^0 from the 2017–18 (a: V1, b: V2, c: V3) and 2018–19 (d: V1, e: V2, f:V3) CAMMPCAN voyages. Observations are shown as the hourly means (dots) ± one standard deviation (error bars).

m^{-3}) but does not replicate the magnitude of the observed enhancement (up to 1.33 ng m^{-3}).

Fig. 8 shows the variability of each PC coincident with variability in the PCR predictions of Hg^0. PC1 had the highest values during V1 in both 2017–18 (Fig. 8a) and 2018–19 (Fig. 8d), meaning the mixing mode was vertically mixing the high-Hg^0 air away from the surface at this time. As the measurements of Hg^0 were collected in situ in surface air, the occurrence of a deeper mixed layer could have dispersed the Hg^0 through the mixed layer and resulted in lower observed concentrations at the surface. This could explain why observations of Hg^0 were lowest when PC1 had the highest values, i.e., during V1 2017–18 and V3 2018–19. An alternative explanation is that the mixing mode of PC1 enhanced tropospheric BrO by lifting bromine-rich air from the surface. This elevated BrO could then have oxidised atmospheric Hg^0, with depleted-Hg^0 air masses mixing through the boundary layer and resulting in the lower surface Hg^0 concentrations observed at this time. During V2 in both 2017–18 (Fig. 8a) and 2018–19 (Fig. 8d), observations of Hg^0 appear anti-correlated with PC1, suggesting the presence of more stable air masses that kept Hg^0 near the surface.

PC2 had the highest values during V3 in both 2017–18 (Fig. 8b) and 2018–19 (Fig. 8e), coincident with some of the highest observed concentrations of Hg^0. Meanwhile, PC2 had the lowest values during V1 2017–18 (Fig. 8b), when Hg^0 was also low. PC2 consists of increased sea ice contact time, high surface wind speed and high relative humidity. The high relative humidity could indicate oceanic air masses with elevated Hg^0 that have been transported across the sea ice, with additional Hg^0 enhancements from snowpack emissions. We previously suggested that high values for PC2 are consistent with favourable conditions for the production of BrO from a blowing snow mechanism (Section 4.4). This could have two possible impacts for Hg^0. First, it could produce BrO that subsequently oxidises Hg^0, consistent with the anti-correlation between Hg^0 and PC2 observed during V3 2018–19 (Fig. 8e) and V2 in 2018–19 (Fig. 8e) but not easily identifiable for V3 in 2017–18 (Fig. 8b). Second, it could enhance the reemission of Hg^0 that was previously deposited to the snowpack or sea ice (Angot et al., 2016a; Humphries et al., 2015), leading to a positive correlation with Hg^0, as observed in V2 2018–19 (Fig. 8b).

PC3 had the highest values during V3 in both 2017–18 (Fig. 8c) and 2018–19 (Fig. 8f) and had an inverse relationship with Hg^0 at these times. PC3 is associated with ocean influence, and the inverse relationship between Hg^0 and PC3 is somewhat unexpected as oceanic biological activity has been found to be a major source for Hg^0 emissions in the Southern Ocean (Cossa et al., 2011). However, the measurements on which that finding was based took place in autumn (March–April), later than our measurements, and may be indicative of different seasonal processes. A likely explanation for the inverse relationship with Hg^0 is that PC3 also provides a source of BrO during the summer months (through either bromocarbons or sea salt aerosol; see Section 4.4), which would in turn decrease Hg^0 concentrations through oxidation.

As mentioned in Section 4.4, while the three principal components

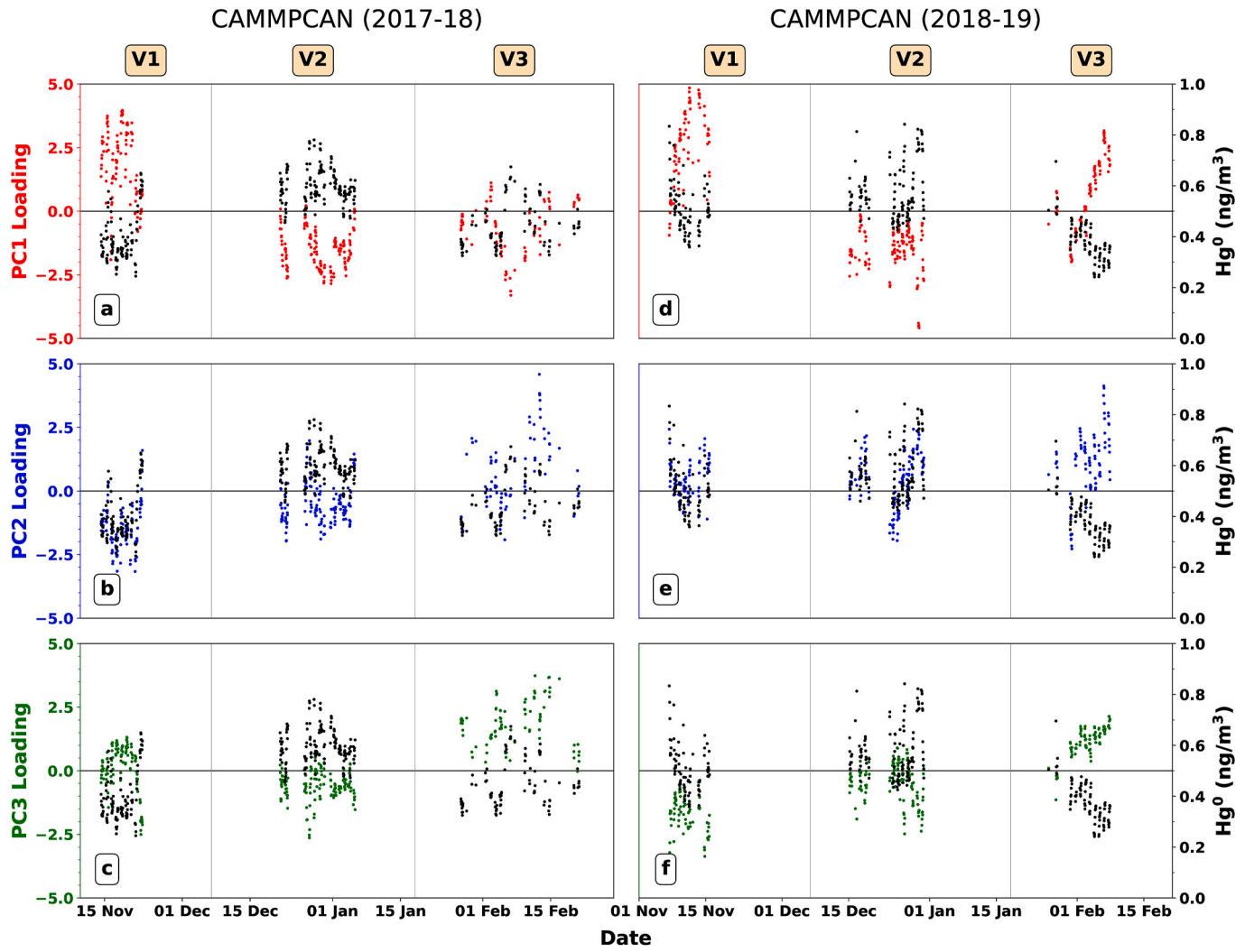

Fig. 8. Same as Fig. 6 but for Hg^0. Here, the black horizontal line shows PC = 0 along with mean observed Hg^0 concentration across all voyages (0.50 ng m^{-3}).

are statistically independent, they work together in the PCR to predict Hg^0. Concurrent influences are particularly evident during V3 2018–19 (Fig. 8f), when there were high values for both PC1 and PC3 along with low values for Hg^0. This could indicate an increased emission of Hg^0 from the ocean source (PC3) but with the concentration of Hg^0 diminished by enhanced vertical mixing throughout the mixed layer (PC1).

5. Conclusion

We analysed the drivers of observed BrO and Hg^0 in the lower troposphere of coastal East Antarctica measured during the CAMMPCAN 2017-19 ship campaign. We found that 14 environmental and meteorological variables had a statistically significant correlation with BrO partial columns and could be used to define statistical modes of Antarctic variability from which we could predict Antarctic BrO and Hg^0.

Using principal component analysis (PCA), we identified three dominant modes of environmental variability in coastal East Antarctica that each have empirical links to BrO sources. PC1 describes a vertical mixing mode, with the conditions necessary to lift air rich in reactive bromine up from the surface and enable formation of BrO through reactions with O_3. PC1 was most important during spring, consistent with the colder temperatures and increased incidence of low-pressure systems at this time of year. PC2 describes a mode associated with blowing snow, driving increased production of sea salt aerosols from blowing snow and subsequent formation of BrO through heterogenous reactions. PC2 was most important during periods of high sea ice cover in spring that coincided with high wind speeds. PC3 describes an ocean influenced mode, possibly associated with the production of bromocarbons from an ocean biological source and/or bromine release from inorganic sea salt aerosols. PC3 was strongest during summer when sea ice cover was reduced.

Comparing our identified Antarctic PCs to the modes identified in the Arctic by Swanson et al. (2020), both have a dominant mode (PC1) that describes low-pressure systems that increase vertical mixing. This consistency implies the importance of low-pressure systems for mixing BrO and its precursors through the boundary layer and lower troposphere is a generalisable polar process. On the other hand, the ocean source mode (PC3) appears unique to the Antarctic dataset, possibly due to the abundance of algae and phytoplankton in the Antarctic as well as the inclusion of summer data in our analysis. Finally, our second Antarctic mode (PC2), which describes conditions favourable for blowing snow events, appears to be similar to the combined effect of the Arctic meteorological (PC1) and chemical (PC3) modes; in our case, the inclusion of sea ice concentration and contact time helps disambiguate the blowing snow contribution.

We used these three dominant modes as drivers in a principal component regression (PCR) to predict Antarctic BrO in the lower troposphere (BrO_{LTcol}). While a previously developed Arctic predictive model (Swanson et al., 2020) performed poorly at predicting Antarctic BrO_{LTcol} with $R^2 < 0.01$, our Antarctic predictive model showed

increased skill with $R = 0.51$ ($R^2 = 0.27$), indicating that key differences exist in the factors that drive BrO variability between the Arctic and Antarctic. We applied the same modes and methodology to predict Antarctic surface Hg^0 concentrations and found that the three dominant modes had higher predictive ability for Hg^0 than for BrO_{LTcol}, with $R = 0.69$ ($R^2 = 0.48$) for the Hg^0 predictions.

Our results reiterate the importance of sea ice as a source of BrO in polar regions. They also highlight the importance of an ocean source for BrO in the Antarctic. While our dataset does not allow us to distinguish between bromocarbons and sea salt aerosols in driving the ocean source, the coastal areas of Antarctica are known hotspots for bromocarbon production due to the upwelling of nutrient rich deep-water that could play a role in tropospheric BrO chemistry (Henley et al., 2017). The differences between bromine cycling in the Arctic and Antarctic and variability of sea-to-air bromocarbon fluxes are not yet fully incorporated into mechanistic models of atmospheric bromine chemistry. Including these Antarctic-specific processes could help to improve model performance and aid the interpretation of future observations in the Antarctic region.

CRediT authorship contribution statement

Neil C. Page: Writing – review & editing, Writing – original draft, Visualization, Methodology, Investigation, Formal analysis. **Jenny A. Fisher:** Writing – review & editing, Supervision, Project administration, Methodology, Funding acquisition, Formal analysis, Conceptualization. **Stephen R. Wilson:** Writing – review & editing, Supervision, Methodology. **Robyn Schofield:** Writing – review & editing, Resources, Project administration, Funding acquisition, Data curation. **Robert G. Ryan:** Writing – review & editing, Data curation. **Sean Gribben:** Writing – review & editing, Data curation. **Andrew R. Klekociuk:** Writing – review & editing, Funding acquisition, Data curation. **Grant C. Edwards:** Data curation. **Anthony Morrison:** Writing – review & editing, Data curation.

Declaration of competing interest

The authors declare that they have no known competing financial interests or personal relationships that could have appeared to influence the work reported in this paper.

Acknowledgements

This work was supported by the Australian Antarctic Division (grant 4431), which funded the CAMMPCAN MAX-DOAS, Hg^0, and O_3 measurements. O_3 measurements during the 2017–18 voyages were supported by the Measurements of Aerosols, Radiation, and Clouds over the Southern Ocean (MARCUS) project. O_3 measurements during the 2018–19 voyages were obtained by a ThermoFisher O_3 monitor provided the University of Wollongong. We thank Clare Paton-Walsh for performing the quality assurance and quality control of the O_3 instrument data. MARCUS data were obtained from the Atmospheric Radiation Measurement (ARM) Program sponsored by the U.S. Department of Energy, Office of Science, Office of Biological and Environmental Research, and Climate and Environmental Sciences Division. We gratefully acknowledge all the CAMMPCAN scientists, ARM technicians and volunteers who were involved with data collection.

Appendix A. Supplementary data

Supplementary data to this article can be found online at https://doi.org/10.1016/j.atmosenv.2024.120918.

Data availability

CAMMPCAN data are available at https://doi.org/10.26179/5e54ab5e5d56f and https://doi.org/10.26179/5e546f452145d. Sea ice cover data are available from the National Snow and Ice Data Center (NSIDC) at https://doi.org/10.7265/N59P2ZTG. MERRA-2 meteorological data are available from NASA/GMAO at https://gmao.gsfc.nasa.gov/reanalysis/MERRA-2/. MARCUS data are available from the DOE ARM archive at https://adc.arm.gov/armlogin/login.jsp.

References

Atmospheric Integrated Research facility for Boundaries and Oxidative eXperiments, 2019. AIRBOX: a mobile chemistry laboratory. Accessed on: 30th March 2021. Available at: https://airbox.earthsci.unimelb.edu.au.

Abrahamsson, K., Granfors, A., Handoff, M., Cuevas, C.A., Saiz-Lopez, A., 2018. Organic bromine compounds produced in sea ice in Antarctic winter. Nat. Commun. 9 (5291). https://doi.org/10.1038/s41467-018-07062-8.

Angot, H., Dastoor, A., De Simone, F., Gardfeldt, K., Gencarelli, C.N., Hedgecock, I.M., Langer, S., Magand, O., Mastromonaco, M.N., Nordstrøm, C., Pfaffhuber, K.A., Pirrone, N., Ryjkov, A., Selin, N.E., Skov, H., Song, S., Sprovieri, F., Steffen, A., Toyota, K., Travnikov, O., Yang, X., Dommergue, A., 2016a. Chemical cycling and deposition of atmospheric mercury in polar regions: review of recent measurements and comparison with models. Atmos. Chem. Phys. 16, 10735–10763. https://doi.org/10.5194/acp-16-10735-2016.

Angot, H., Dion, I., Vogel, N., Legrand, M., Magand, O., Dommergue, A., 2016b. Multi-year record of atmospheric mercury at Dumont d'Urville, East Antarctic coast: continental outflow and oceanic influences. Atmos. Chem. Phys. 16, 8265–8279. https://doi.org/10.5194/acp-16-8265-2016.

Bognar, K., Zhao, X., Strong, K., Chang, R.Y.-W., Frieß, U., Hayes, P.L., McClure-Begley, A., Morris, S., Tremblay, S., Vicente-Luis, A., 2020. Measurements of tropospheric bromine monoxide over four halogen activation seasons in the Canadian high Arctic. JGR: Atmosphere. https://doi.org/10.1029/2020JD033015.

Burgay, F., Fernández, R.P., Segato, S., Turetta, C., Blaszczak-Boxe, C.S., Rhodes, R.H., Scarchilli, C., Ciardini, V., Barbante, C., Saiz-Lopez, A., Spolaor, A., 2023. 200-year ice core bromine reconstruction at Dome C (Antarctica): observational and modelling results. Cryosphere 17, 391–405. https://doi.org/10.5194/tc-17-391-2023.

Cairns, W.R.L., Turetta, C., Maffezzoli, N., Magand, O., Araujo, B.F., Angot, H., Segato, D., Cristofanelli, P., Sprovieri, F., Scarchilli, C., Grigioni, P., Ciardini, V., Barbante, A., Dommergue, A., Spolaor, A., 2021. Mercury in precipitated and surface snow at Dome C and a first estimate of mercury depositional fluxes during the Austral summer on the high Antarctic plateau. Atmos. Environ. 262. https://doi.org/10.1016/j.atmosenv.2021.118634.

Chambers, S.D., Choi, T., Park, S.J., Williams, A.G., Hong, S.B., Tositti, L., Griffiths, A.D., Crawford, J., Pereira, E., 2017. Investigating local and remote terrestrial influence on air masses at contrasting antarctic sites using radon-222 and back trajectories. J. Geophys. Res. Atmos. 122, 13525–13544. https://doi.org/10.1002/2017JD026833.

Cossa, D., Heimburger, L.-E., Lannuzel, D., Rintoul, S.R., Butler, E.C.V., Bowie, A.R., Averty, B., Watson, R.J., Remenyi, T., 2011. Mercury in the Southern Ocean. Geochem. Cosmochim. Acta 75, 4037–4052. https://doi.org/10.1016/j.gca.2011.05.001.

Danckaert, T., et al., 2017. QDOAS Software User Manual. Royal Belgian Institute for Space Aeronomy, p. 123. Available at: http://uv-vis.aeronomie.be/software/QDOAS.

Draxler, R.R., 1999. HYSPLIT4 user's guide. In: NOAA Tech. Memo. ERL ARL-230. NOAA Air Resources Laboratory, Silver Spring, MD.

Draxler, R.R., Hess, G.D., 1997. Description of the HYSPLIT_4 modeling system. NOAA Tech. Memo. ERL ARL-224. NOAA Air Resources Laboratory, Silver Spring, MD, p. 24.

Draxler, R.R., Hess, G.D., 1998. An overview of the HYSPLIT_4 modeling system of trajectories, dispersion, and deposition. Aust. Meteorol. Mag. 47, 295–308.

Fisher, J.A., Schneider, L., Fostier, A.-H., Guerrero, S., Guimarães, J.R.D., Labuschagne, C., Leaner, J.J., Martin, L.G., Mason, R.P., Somerset, V., Walters, C., 2023. A synthesis of mercury research in the Southern Hemisphere, part 2: anthropogenic perturbations. Ambio 52, 918. https://doi.org/10.1007/s13280-023-01840-5, 237.

Frey, M.M., Norris, S.J., Brooks, I.M., Anderson, P.S., Nishimura, K., Yang, X., Jones, A. E., Nerentorp Mastromonaco, M.G., Jones, D.H., Wolff, E.W., 2020. First direct observation of sea salt aerosol production from blowing snow above sea ice. Atmos. Chem. Phys. 20, 2549–2578. https://doi.org/10.5194/acp-20-2549-2020.

Frieß, U., Monks, P.S., Remedios, J.J., Rozanov, A., Sinreich, R., Wagner, T., Platt, U., 2006. MAX-DOAS O4 measurements/A new technique to derive information on

atmospheric aerosols/2. Modeling studies. J. Geophys. Res. 111. https://doi.org/10.1029/2005JD006618, 20pp.
Frieß, U., Deutschmann, T., Gilfedder, B.S., Weller, R., Platt, U., 2010. Iodine monoxide in the Antarctic snowpack. Atmos. Chem. Phys. 10, 2439–2456. https://doi.org/10.5194/acp-10-2439-2010.
Frieβ, U., Sihler, H., Sander, R., Phler, D., Yilmaz, S., Platt, U., 2011. The vertical distribution of BrO and aerosols in the Arctic: measurements by active and passive differential optical absorption spectroscopy. J. Geophys. Res. Atmos. 116 (18), 1–19. https://doi.org/10.1029/2011JD015938.
Frieß, U., Kreher, K., Querel, R., Schmithüsen, H., Smale, D., Weller, R., Platt, U., 2023. Source mechanisms and transport patterns of tropospheric bromine monoxide: findings from long-term multi-axis differential optical absorption spectroscopy measurements at two Antarctic stations. Atmos. Chem. Phys. 23, 3207–3232. https://doi.org/10.5194/acp-23-3207-2023.
Gelaro, R., McCarty, W., Suarez, M.J., Todling, R., Molod, A., Takacs, L., Randles, C.A., Darmenov, A., Bosilovich, M.G., Reichle, R., Wargan, K., Coy, L., Cullather, R., Ddraper, C., Akella, S., Buchard, V., Conaty, A., Da Silva, A.M., Gu, W., Kim, G.-K., Koster, R., Lucchesi, R., Merkova, D., Nielsen, J.E., Partyka, G., Pawson, S., Putman, W., Rienecker, M., Schubert, S.D., Sienkiewicz, M., Zhao, B., 2017. The modern-Era Retrospective analysis for research and Applications. J. Clim. 30, 5419–5454. https://doi.org/10.1175/JCLI-D-16-0758.1.
Gionfriddo, C.M., Tate, M.T., Wick, R.R., Schultz, M.B., Zemla, A., Thelen, M.P., Schofield, R., Krabbenhoft, D.P., Holt, K.E., Moreau, J.W., 2016. Microbial mercury methylation in Antarctic sea ice. Nat. Microbiol. 1 (10), 16127. https://doi.org/10.1038/nmicrobiol.2016.127.
Giordano, M.R., Kalnajs, L.E., Goetz, J.D., Avery, A.M., Katz, E., May, N.W., Leemon, A., Mattson, C., Pratt, K.A., DeCarlo, P.F., 2018. The importance of blowing snow to halogen-containing aerosol in coastal Antarctica: influence of source region versus wind speed. Atmos. Chem. Phys. 18, 16689–16711. https://doi.org/10.5194/acp-18-16689-2018.
Halfacre, J.W., Shepson, P.B., Pratt, K.A., 2019. pH-dependent production of molecular chlorine, bromine, and iodine from frozen saline surfaces. Atmos. Chem. Phys. 19, 4917–4931. https://doi.org/10.5194/acp-14-4875-2014.
Hara, K., Osada, K., Yabuki, M., Matoba, S., Hirabayashi, M., Fujita, S., Nakazawa, F., Yamanouchi, T., 2020. Atmospheric sea-salt and halogen cycles in the Antarctic. Env. Sci.: Process. Impacts 10. https://doi.org/10.1039/D0EM00092B.
Hay, T.D., 2011. MAX-DOAS Measurements of Bromine Explosion Events in McMurdo Sound, Antarctica. University of Canterbury, New Zealand.
Helmig, D., Johnson, B., Oltmans, S.J., Neff, W., Eisele, F., Davis, D.D., 2008. Elevated ozone in the boundary layer at South pole. Atmos. Environ. 42 (12), 2788–2803.
Henley, S.F., Tuerena, R.E., Annett, A.L., Fallick, A.E., Meredith, M.P., Venables, H.J., Clarke, A., Ganeshram, R.S., 2017. Macronutrient supply, uptake and recycling in the coastal ocean of the west Antarctic Peninsula. Deep Sea Res. Part II Top. Stud. Oceanogr. 139, 58–76. https://doi.org/10.1016/j.dsr2.2016.10.003.
Herrmann, M., Cao, L., Sihler, H., Platt, U., Gutheil, E., 2019. On the contribution of chemical oscillations to ozone depletion events in the polar spring. Atmos. Chem. Phys. 19, 10161–10190. https://doi.org/10.5194/acp-19-10161-2019.
Hönninger, G., Platt, U., 2002. Observations of BrO and its vertical distribution during surface ozone depletion at Alert. Atmos. Environ. 36, 2481–2489. https://doi.org/10.1016/S1352-2310(02)00104-8.
Hossaini, R., Mantle, H., Chipperfield, M.P., Montzka, S.A., Hamer, P., Ziska, F., Quack, B., Krüger, K., Tegtmeier, S., Atlas, E., Sala, S., Engel, A., Bönisch, H., Keber, T., Oram, D., Mills, G., Ordóñez, C., Saiz-Lopez, A., Warwick, N., Liang, Q., Feng, W., Moore, F., Miller, B.R., Marécal, V., Richards, N.A.D., Dorf, M., Pfeilsticker, K., 2013. Evaluating global emission inventories of biogenic bromocarbons. Atmos. Chem. Phys. 13, 11819–11838. https://doi.org/10.5194/acp-13-11819-2013.
Huang, J., Jaeglé, L., 2017. Wintertime enhancements of sea salt aerosol in polar regions consistent with a sea ice source from blowing snow. Atmos. Chem. Phys. 17, 3699–3712. https://doi.org/10.5194/acp-17-3699-2017.
Huang, J., Jaeglé, L., Chen, Q., Alexander, B., Sherwen, T., Evans, M.J., Theys, N., Choi, S., 2020. Evaluating the impact of blowing-snow sea salt aerosol on springtime BrO and O_3 in the Arctic. Atmos. Chem. Phys. 20, 7335–7358. https://doi.org/10.5194/acp-20-7335-2020.
Hughes, C., Chuck, A.L., Rossetti, H., Mann, P.J., Turner, S.M., Clarke, A., Chance, R., Liss, P.S., 2009. Seasonal cycle of seawater bromoform and dibromomethane concentrations in a coastal bay on the western Antarctic Peninsula. Global Biogeochem. Cycles 23, GB2024. https://doi.org/10.1029/2008GB003268.
Hughes, C., Johnson, M., von Glasow, R., Chance, R., Atkinson, H., Souster, T., Lee, G.A., Clarke, A., Meredith, M., Venables, M.J., Turner, S.M., Malin, G., Liss, P.S., 2012. Climate-induced change in biogenic bromine emissions from the Antarctic marine biosphere. Global Biogeochem. Cycles 26, GB3019. https://doi.org/10.1029/2012GB004295.
Hughes, C., Johnson, M., Utting, R., turner, S., Malin, G., Clarke, A., Liss, P.S., 2013. Microbial control of bromocarbon concentrations in coastal waters of the western Antarctic Peninsula. J. Marine Chem. 151, 35–46. https://doi.org/10.1016/j.marchem.2013.01.007.
Humphries, R.S.S., Schofield, R., Keywood, M.D., Ward, J., Pierce, J.R.R., Gionfriddo, C. M.M., Tate, M.T., Krabbenhoft, D.P., Galbally, I.E.E., Molloy, S.B.B., Klekociuk, A.R., Johnston, P.V.V., Kreher, K., Thomas, A.J.J., Robinson, A.D.D., Harris, N.R.P.R.P., Johnson, R., Wilson, S.R.R., 2015. Boundary layer new particle formation over East Antarctic sea ice - possible Hg driven nucleation? Atmos. Chem. Phys. 15, 13339–13364. https://doi.org/10.5194/acpd-15-19477-2015.
Jones, A.E., Anderson, P.S., Begoin, M., Brough, N., Hutterli, M.A., Marshall, G.J., Richter, A., Roscoe, H.K., Wolff, E.W., 2009. BrO, blizzards, and drivers of polar tropospheric ozone depletion events. Atmos. Chem. Phys. 9 (14), 4639–4652. https://doi.org/10.5194/acp-9-4639-2009.
Jones, A.E., Anderson, P.S., Wolff, E.W., Roscoe, H.K., Marshall, G.J., Richter, A., Brough, N., Colwell, S.R., 2010. Vertical structure of Antarctic tropospheric ozone depletion events: characteristics and broader implications. Atmos. Chem. Phys. 10, 7775–7794. https://doi.org/10.5194/acp-10-7775-2010.
Kukui, et al., 2014. Measurements of OH and RO2 radicals at dome C, East Antarctica. Atmos. Chem. Phys. 14, 12373–12392. https://doi.org/10.5194/acp-14-12373-2014.
Lieb-Lappen, R.M., Obbard, R.W., 2015. The role of blowing snow in the activation of bromine over first-year Antarctic sea ice. Atmos. Chem. Phys. 15, 7537–7545. https://doi.org/10.5194/acp-15-7537-2015.
Mardia, K.V., Kent, J.T., Bibby, J.M., 1979. Multivariate Analysis. Academic Press, London.
McGrath-Spangler, E.L., Molod, A., 2014. Comparison of GEOS-5 AGCM planetary boundary layer depths computed with various definitions. Atmos. Chem. Phys. 14, 6717–6727. https://doi.org/10.5194/acp-14-6717-2014.
Meier, W.N., Fetterer, F., Savoie, M., Mallory, S., Duerr, R., Stroeve, J., 2017. NOAA/NSIDC Climate Data Record of Passive Microwave Sea Ice Concentration, Version 3. [Oct 2017 to Mar 2019]. NSIDC: National Snow and Ice Data Center, Boulder, Colorado USA. https://doi.org/10.7265/N59P2ZTG. Accessed: 16 September 2019.
Moore, C.W., Obrist, D., Steffen, A., Staebler, R.M., Douglas, T.A., Richter, A., Nghiem, S. V., 2014. Convective forcing of mercury and ozone in the Arctic boundary layer induced by leads in sea ice. Nature 506, 81–84. https://doi.org/10.1038/nature12924.
Nygård, T., Valkonen, T., Vihma, T., 2013. Antarctic low-tropospheric humidity inversions: 10-yr climatology. J. Clim. 26, 5205–5219.
Pang, Q., Gu, J., Wang, H., Zhang, Y., 2022. Global health impact of atmospheric mercury emissions from artisanal and small-scale gold mining. iScience 25 (9), 104881. https://doi.org/10.1016/j.isci.2022.104881.
Peterson, P.K., Simpson, W.R., Pratt, K.a., Shepson, P.B., Frieß, U., Zielcke, J., Platt, U., Walsh, S.J., Nghiem, S.V., 2015. Dependence of the vertical distribution of bromine monoxide in the lower troposphere on meteorological factors such as wind speed and stability. Atmos. Chem. Phys. 15, 2119–2137. https://doi.org/10.5194/acp-15-2119-2015.
Peterson, P.K., Hartwig, I.M., May, N.W., Schwartz, E., Rigor, I., Ermold, W., Steele, M., Morison, J.H., Nghiem, S.V., Pratt, K.A., 2019. Snowpack measurements suggest role for multi-year sea ice regions in Arctic atmospheric bromine and chlorine chemistry. Elem. Sci. Anthrop. 7 (14). https://doi.org/10.1525/elementa.352.
Pöhler, D., Vogel, L., Friess, U., Platt, U., 2010. Observation of halogen species in the Amundsen Gulf, Arctic, by active long-path differential optical absorption spectroscopy. Proc. Natl. Acad. Sci. U.S.A. 107 (15), 6582–6587. https://doi.org/10.1073/pnas.0912231107.
Prados-Roman, C., Gómez-Martín, L., Puentedura, O., Navarro-Comas, M., Iglesias, J., de Mingo, J.R., Pérez, M., Ochoa, H., Barlasina, M.E., Carbajal, G., Yela, M., 2018. Reactive bromine in the low troposphere of Antarctica. Estimations at two research sites. Atmos. Chem. Phys. 18, 8549–8570. https://doi.org/10.5194/acp-18-8549-2018.
Pratt, K.A., Custard, K.D., Shepson, P.B., Douglas, T.A., Pöhler, D., General, S., et al., 2013. Photochemical production of molecular bromine in Arctic surface snowpacks. Nat. Geosci. 6 (5), 351–356. https://doi.org/10.1038/ngeo1779.
Rhodes, R.H., Yang, X., Wolff, E.W., McConnell, J.R., Frey, M.M., 2017. Sea ice as a source of sea salt aerosol to Greenland ice cores: a model-based study. Atmos. Chem. Phys. 17, 9417–9433. https://doi.org/10.5194/acp-17-9417-2017.
Rogerson, P.A., 2001. Statistical Methods for Geography. SAGE Publications, Ltd. https://doi.org/10.4135/9781849209953.
Rozanov, V., Rozanov, A., Kokhanovsky, A., Burrows, J., 2014. Radiative transfer through terrestrial atmosphere and ocean: software package SCIATRAN. J. Quant. Spectrosc. Radiat. Transf. 133, 13–71.
Saiz-Lopez, A., Mahajan, A.S., Salmon, R.A., Bauguitte, S.J., Jones, A.E., Roscoe, H.K., Plane, J., 2007. Boundary layer halogens in coastal Antarctica. Science 317, 348–351. https://doi.org/10.1126/science.1141408.
Schlosser, E., Powers, J.G., Duda, M.G., Manning, K.W., 2011. Interaction between Antarctic sea ice and synoptic activity in the circumpolar trough: implications for ice-core interpretation. Ann. Glaciol. 52 (57), 9–17. https://doi.org/10.3189/172756411795931859, 2011.
Schofield, R., Ryan, R.G., 2021a. Observations Collected Aboard Aurora Australis by AIRBOX and Associated Instruments – 2017-18 Season, Ver. 1, Australian Antarctic Data Centre -. https://doi.org/10.26179/5e54ab5e5d56f.
Schofield, R., Ryan, R.G., 2021b. Observations Collected between 18th October 2018 and 29th March 2019 Aboard Aurora Australis by AIRBOX and Associated Instruments, Ver. 1, Australian Antarctic Data Centre. https://doi.org/10.26179/5e546f452145d.
Seibert, P., Beyrich, F., Gryning, S., Jo, S., Rasmussen, A., Tercier, P., 2000. Review and intercomparison of the operational methods for the determination of mixing height. Atmos. Environ. 34 (7), 1001–1027. https://doi.org/10.1016/S1352-2310(99)00349-0.
Seo, S., Richter, A., Blechschmidt, A.-M., Bougoudis, I., Burrows, J.P., 2020. Spatial distribution of enhanced BrO and its relation to meteorological parameters in Arctic and Antarctic sea ice regions. Atmos. Chem. Phys. 20, 12285–12312. https://doi.org/10.5194/acp-20-12285-2020.
Shapiro, S.S., Wilk, M.B., 1965. An analysis of variance test for normality (complete samples). Biometrika 52 (3–4), 591–611. https://doi.org/10.1093/biomet/52.3-4.591.
Simpson, W.R., Brown, S.S., Saiz-Lopez, A., Thornton, J.A., Von Glasow, R., 2015. Tropospheric halogen chemistry: sources, cycling, and impacts. In: Chemical

Reviews, vol. 115, pp. 4035–4062. https://doi.org/10.1021/cr5006638. American Chemical Society, Issue 10.
Simpson, W.R., Peterson, P.K., Frieß, U., Sihler, H., Lampel, J., Platt, U., Moore, C., Pratt, K., Shepson, P., Halfacre, J., Nghiem, S.V., 2017. Horizontal and vertical structure of reactive bromine events probed by bromine monoxide MAX-DOAS. Atmos. Chem. Phys. 17, 9291–9309. https://doi.org/10.5194/acp-17-9291-2017.
Simpson, W.R., Frieß, U., Thomas, J.L., Lampel, J., Platt, U., 2018. Polar nighttime chemistry produces intense reactive bromine events. Geophys. Res. Lett. 45, 9987–9994. https://doi.org/10.1029/2018GL079444.
Slusher, D.L., Neff, W.D., Kim, S., Huey, L.G., Wang, Y., Zeng, T., Tanner, D.J., Blake, D. R., Beyersdorf, A., Lefer, B.L., Crawford, J.H., Eisele, F.L., Mauldin, R.L., Kosiuch, E., Buhr, M.P., Wallace, H.W., Davis, D.D., 2010. Atmospheric chemistry results from the ANTCI 2005 Antarctic plateau airborne study. J. Geophys. Res. Atmos. 115, D07304. https://doi.org/10.1029/2009JD012605.
Song, S., Angot, H., Selin, N.E., Gallée, H., Sprovieri, F., Pirrone, N., Helmig, D., Savarino, J., Magand, O., Dommergue, A., 2018. Understanding mercury oxidation and air-snow exchange on the East Antarctic Plateau: a modeling study. Atmos. Chem. Phys. 18, 15825–15840. https://doi.org/10.5194/acp-18-15825-2018.
Steffen, A., Scherz, T., Olson, M., Gay, D., Blanchard, P., 2012. A comparison of data quality control protocols for atmospheric mercury speciation measurements. J. Environ. Monit. 14, 752–765. https://doi.org/10.1039/c2em10735j.
Stein, A.F., Draxler, R.R., Rolph, G.D., Stunder, B.J.B., Cohen, M.D., Ngan, F., 2015. NOAA's HYSPLIT atmospheric transport and dispersion modeling system. Bull. Am. Meteorol. Soc. 96, 2059–2077. https://doi.org/10.1175/BAMS-D-14-00110.1.
Swanson, W.F., Graham, K.A., Halfacre, J.W., Holmes, C.D., Shepson, P.B., Simpson, W. R., 2020. Arctic reactive bromine events occur in two distinct sets of environmental conditions: a statistical analysis of 6 Years of observations. J. Geophys. Res., [Atmos.] 125 (10), 1–19. https://doi.org/10.1029/2019JD032139.
Symons, L., 2018a. Aurora Australis Voyage 1 2017/18 Track and Underway Data. Australian Antarctic Data Centre - CAASM Metadata. Accessed: 11th October 2018. Available at: https://data.aad.gov.au/metadata/records/201718010.
Symons, L., 2018b. Aurora Australis Voyage 2 2017/18 Track and Underway Data. Australian Antarctic Data Centre - CAASM Metadata. Accessed: 11th October 2018. Available at: https://data.aad.gov.au/metadata/records/201718020.
Symons, L., 2018c. Aurora Australis Voyage 3 2017/18 Track and Underway Data. Australian Antarctic Data Centre - CAASM Metadata. Accessed: 11th October 2018. Available at: https://data.aad.gov.au/metadata/records/201718030.
Symons, L., 2019a. Aurora Australis voyage 1 2018/19 track and underway data Australian antarctic data Centre - CAASM metadata. Accessed: 16th July 2019. Available at: https://data.aad.gov.au/metadata/records/201819010.
Symons, L., 2019b. Aurora Australis voyage 2 2018/19 track and underway data Australian antarctic data Centre - CAASM metadata. Accessed: 16th July 2019. Available at: https://data.aad.gov.au/metadata/records/201819020.
Symons, L., 2019c. Aurora Australis voyage 3 2018/19 track and underway data Australian antarctic data Centre - CAASM metadata. Accessed: 16th July 2019. Available at: https://data.aad.gov.au/metadata/records/201819030.
Unagar, A., Hashmi, A., Tiwari, A.K., Jawak, S.D., Desai, B., Urba, A., Qureshi, A., 2021. Coast of Eastern Antarctica as the source of atmospheric mercury during austral summer. Atmos. Pollut. Res. 12, 101226. https://doi.org/10.1016/j.apr.2021.101226.
U.S Department of Energy's Atmospheric Radiation Measurement (ARM) program, 2019. Measurements of aerosol, radiation, and Clouds over the Southern Ocean (MARCUS). Accessed on: 12th March 2019. Available at: https://www.arm.gov/research/campaigns/amf2017marcus.
Vancoppenolle, M., Fichefet, T., Bitz, C.M., 2006. Modeling the salinity profile of undeformed Arctic sea ice. Geophys. Res. Lett. 33, L21501. https://doi.org/10.1029/2006GL028342.
Wagh, S.P., Joge, S.D., Singh, S., Mali, P., Beirle, S., Wagner, T., Bucci, S., Saiz-Lopez, A., Bhawar, R., Mahajan, A.S., 2023. Year-long ground-based observations of bromine oxide over Bharati Station, Antarctica. Polar Sci. 38, 100977. https://doi.org/10.1016/J.POLAR.2023.100977.
Yang, X., Frey, M.M., Rhodes, R.H., Norris, S.J., Brooks, I.M., Anderson, P.S., Nishimura, K., Jones, A.E., Wolff, E.W., 2019. Sea salt aerosol production via sublimating wind-blown saline snow particles over sea ice: parameterizations and relevant microphysical mechanisms. Atmos. Chem. Phys. 19 (13), 8407–8424. https://doi.org/10.5194/acp-19-8407-2019.